I. INTRODUCTION

To understand star formation in spiral arms and to test the predictions of spiral density wave models, we present a detailed observational study of the grand-design spiral M81. For testing theories of global spiral structure, M81 has distinct advantages: (a) it has a dominant global two-armed pattern; (b) it is easily resolved and has an inclination suitable for dynamical studies; (c) the H I velocity contours show a sharp velocity discontinuity identified as a spiral velocity shock (Visser 1980a, b; Hine 1984; Hine and Rots 1989), which provides strong evidence for a nonlinear density wave in the H I gas; (d) the I-band photograph in Elmegreen (1981) and the azimuthal profiles in Schweizer (1976) reveal a stellar density wave in the old disk stars; and (e) theoretical density wave models of this galaxy are available from Visser and from Leisawitz and Bash (1982) for easy comparison with observations.

There are two components to our study. First, we wish to use only observed quantities such as the location of the H II regions with respect to the observed H I velocity discontinuity. Independent of any theory for the cause of spiral structure in galaxies, it seems important to see where new stars lie along the spiral arms. Second, we want to determine which of the characteristics predicted by the various theories for spiral structure are actually found in M81 and which are not.

There are various theoretical models of how a galaxy responds to a spiral density wave. The hydrodynamic calculations of Roberts (1969), Visser (1980a, b), and van Albada (1985), for example, treat the interstellar gas as a continuous, single-component medium and predict a shock front along the inside edge of the spiral arm. Other density wave models (e.g., Leisawitz and Bash 1982; Roberts and Hausman 1984; Combes and Gerin 1985; Tomisaka 1987; Roberts and Stewart 1987) try to take account of the obvious clumpy nature of the interstellar medium. These cloudy models differ from one another in the assumptions made about how giant clouds are formed and about the role played by cloud collisions. Indeed, in the cloudy model of Roberts and Hausman, cloud collisions trigger star formation. In the ballistic particle model of Leisawitz and Bash, the energy input from collisions between giant clouds and small H I clouds delays the onset of star formation in the GMCs. In the models of Tomisaka (1987) and Combes and Gerin (1985), the principal role of cloud collisions is to form larger clouds by coalescence. Roberts and Hausman and Roberts and Stewart (1987) assume that clouds always exist as entities; they use an N-body calculation to simulate the motions of the clouds. Roberts and Hausman (1984) find that their cloudy model produces a spiral density enhancement about 1 kpc wide and a spiral "shock front" 300–600 pc wide; this is much broader than the shock width predicted by Visser's (1980b) fluid model. Roberts and Stewart find that the clouds temporarily group to create loose "GMC–like" aggregations in the arms as a result of orbit crowding near the potential minimum. The models by Roberts and coworkers are incomplete in that they do not consider how to replenish the supply of clouds after clumps are destroyed by star formation. On the other hand, Leisawitz and Bash adopt Visser's fluid model for the H I gas in M81 but add to this a set of giant clouds that orbit ballistically. They postulate that the giant clouds are formed at the spiral shock front and are launched at velocities close to the post shock velocity in Visser's model.

Elmegreen (1987) points out that different components of the interstellar gas may respond differently to a density wave. He notes that small (diffuse) H I clouds have short mean free paths in the spiral arm, and thus an ensemble of small clouds behaves as a continuous fluid that may undergo a spiral shock; giant clouds may have long mean free paths and behave instead like ballistic particles.

We find it useful to consider three levels of clouds in M81; (1) an ensemble of small H I clouds that exhibits a spiral velocity shock; (2) large H I clouds (also called "clumps") that orbit ballistically and serve as the "particles" in the N-body calculations by Roberts and coworkers; and (3) the giant clouds in which the giant radio H II complexes occur. The large clouds can account for the broad H I arms that Hine and Rots (1989) detect in M81. In the models by Roberts and coworkers, the giant clouds are formed by (perhaps temporary) agglomeration of large clouds.

It is important to subject these various models and suggestions to observational tests. For M81 we have high-resolution digitized images that enable us to study in detail the following spiral tracers: the young stars, the giant H II regions, the older stars, the dust lanes, the H I surface density, the H I velocity shock front, and the radio continuum arms. The digitized images consist of H I intensity and velocity maps from Hine and Rots (1989), B and I plates from Elmegreen (1981), radio continuum maps from Bash and Kaufman (1986), and Hα observations described in Kaufman et al. (1987). The radio continuum and H I data were both taken at the VLA.[2] The radio and optical maps are all registered to the same coordinate grid and have point-spread functions in the range 7"–10" (FWHM). We easily resolve the spiral arms. We adopt a distance of 3.3 Mpc for M81 from Bottinelli et al. (1984); then the corresponding linear resolution is 110–160 pc. Kaufman et al. (1987) identify 42 giant H II regions with high surface brightness that are detected in the radio continuum maps of M81. These are referred to here as "giant radio H II regions,"

This set of images allows us to test density wave models in ways not possible before. We present two types of information about the spiral tracers: namely, (1) where are the various tracers located with respect to each other in a face-on image, and (2) how do various tracers compare in surface density or surface brightness? In particular, we measure the displacement of each tracer from the observed spiral velocity shock front (seen in the H I map), and check on whether common notions about grand design spirals (such as the relative location of the nonthermal radio arms and the shock front) are valid for M81. The displacements of the giant radio H II regions from the shock front are useful for constraining assumptions about where the giant clouds form in the galaxy, how such clouds travel across the arm, and when OB associations are created. Kaufman and Bash (1987) report that the observed locations of the giant radio H II regions conflict with the predictions of Leisawitz and Bash (1982). The quantitative results are presented here.

This paper is organized as follows. In § II we briefly describe the observational material used. In § III we use the data to specify the locations of the spiral shock front, the inner Lindblad resonance, and the gravitational potential minimum on the arms. We measure the displacements of the various spiral tracers from the observed shock front as a function of galactocentric radius R. In § IV we discuss the locations of the giant

radio H II regions in more detail and compare with the predictions of cloudy models. In § V we describe where the nonthermal radio arms are located relative to other spiral tracers and compare surface brightness trends along the arms. We set limits on the ratio of nonthermal to free-free radio emission from the spiral arms and discuss whether the observations are consistent with an SNR origin for the cosmic-ray electrons. In § VI, we see if there is a detailed correspondence between the giant radio H II regions and the H I concentrations. In particular, we test whether the Lyman continuum flux is related to the H I column density. In § VII we use a comparison of the visual extinction A_v and the H I column density to infer information about molecular gas in the directions of the giant radio H II regions. We summarize our conclusions in § VIII.

II. THE DIGITIZED IMAGES

The individual optical and radio observations are described in detail by Elmegreen (1981), Hine (1984), Bash and Kaufman (1986), and Kaufman *et al.* (1987), respectively. To transform to face-on images, we adopt an inclination, i, of 59° and a position angle of 149° for the major axis, to be consistent with Visser (1980a, b) and Leisawitz and Bash (1982). Figure 1 (Plate 7) displays the face-on digitized maps of the H I surface density, the $\lambda = 20$ cm radio continuum emission, the younger stars, and the giant radio H II regions. Pseudo-color versions of these images are presented by Kaufman (1987). All four pictures in Figure 1 depict the same field on the same scale. The major axis is horizontal with the eastern arm on the right and the northern major axis on the left. (Ignore the nucleus in all the figures in this paper.)

To remove the older stars and produce the image labeled "younger stars," we subtracted the I-band surface brightness from the B-band surface brightness. All the radio and optical maps are registered to the same coordinate grid. For the optical images (Hα, B, and I plates) this involved doing plate solutions and transforming the digitized maps to α, δ coordinates as in Kaufman *et al.* (1987). The plate solutions have standard deviations less than the adopted pixel size of 1".9 (30 pc). The registered images, which are used for the position measurements in § III, have point spread functions ranging in FWHM from 7" for the B and I images to 9" for the H I image to 10" for the radio continuum image. However, for the display in Figure 1, the 20 cm radio continuum map was convolved to a 15" beam to increase sensitivity; this did not affect the measured location of the inside edge of the arm.

III. LOCATION OF THE MAIN DENSITY WAVE FEATURES

In this section the locations of the spiral shock front, the inner Lindblad Resonance (ILR), and the gravitational potential minimum are specified from the observations.

a) The Spiral Shock Front

Hine (1984) determines the position of the shock front in the H I gas from the VLA observations of Hine and Rots (1989). For galactocentric radius $R \geq 5$ kpc, Hine provides for each arm three estimates of the location of the shock front at each value of R: two estimates from the velocity data and one from the abrupt increase in the H I surface density at the inside edge of the arm. For the latter he chooses the location halfway up the steep slope. There is no systematic difference between the shock position given by the sudden increase in H I surface density and that given by the velocity discontinuity. Over the range $R = 5.0$–9.5 kpc, the average dispersion in spiral phase

angle η (defined in eq. [5] below) for his three estimates is 7° (western arm) and 6° (eastern arm). For $R < 5$ kpc Hine uses only the H I surface density data to determine the shock position.

The spiral curves in Figure 2 (Plate 8) mark the position of Hine's fitted shock front, which is overlayed on the face-on images of Figure 1. The sharp kinks in his fitted curves at $R = 7$ kpc are artificial, the result of joining two splines, but the pitch angle does change near this radius.

b) Displacements from the Shock Front

It is clear from the pictures in Figure 2 that the giant radio H II regions, the ridge of younger stars along the arms, and, for the most part, the radio continuum emission from the arms all lie downstream from the spiral shock front. To clarify the nomenclature used below, we remind the reader of the rudiments of density wave theory. In classical density wave models for M81, the spiral arms lie between the inner Lindblad resonance and corotation, where the angular speed Ω of galactic rotation equals the angular speed Ω_p of the spiral pattern. Interior to corotation, the material (gas, stars, dust) travels faster than the spiral pattern. Since the sense of rotation is such that the arms trail, the material will enter the arm on the inside edge and leave the arm on the outside edge. The material flowing through the arm is "upstream" on the inside edge of the arm and "downstream" on the outside edge. If stars were to form at the spiral shock front and travel at the local circular velocity of galactic rotation, then the young stars would be downstream from the shock front, i.e., toward the outside edge of the arm.

To describe the observed displacements quantitatively, we present a series of graphs showing the locations of the spiral arms defined by the various spiral tracers, Specifically, in the polar coordinate plots of Figure 3, we show the positions in a face-on image of (1) the spiral shock front (as a heavy solid line), (2) the ridges of peak H I surface density, (3) the giant radio H II regions, (4) the ridges of peak surface brightness on the younger stars image, (5) the ridges of peak surface brightness on the I-band image, and (6) the dust lanes. The dust lane positions were measured on the digitized B image. The dust lanes are discussed in more detail by Kaufman, Elmegreen, and Bash (1989). The azimuthal angle θ is measured counterclockwise from the southern major axis; downstream is in the direction of increasing θ. The positions of the giant radio H II regions are accurate to ± 1 pixel (1".9), and the positions of the ridges on the H I, younger star, and I-band images are accurate to ± 1–2 pixels. At the location of the spiral arms, a 1 pixel uncertainty corresponds to uncertainties $\Delta R = 30$ pc, $\Delta \theta = 0°.7$ near the major axis ($R \cong 5$ kpc) and to $\Delta R = 60$ pc, $\Delta \theta = 0°.2$ near the minor axis ($R \cong 8$ kpc).

Because our goal is to study interrelationships between these spiral tracers, we present here the entire set of graphs showing the displacements from the spiral shock front and then discuss the separate features in the sections below. In addition to the main continuous ridge along each arm, the positions plotted for the H I, I-band and younger star images include a few spurs jutting out from the arm plus some other features.

c) The Inner Lindblad Resonance

The two main H I arms emerge from a faint inner ring at $R = 4.0 \pm 0.2$ kpc (see the VLA H I image in Figs. 1 and 2). Rots (1975) points out the H I ring in his lower resolution WSRT observations and suggests that it may be produced by
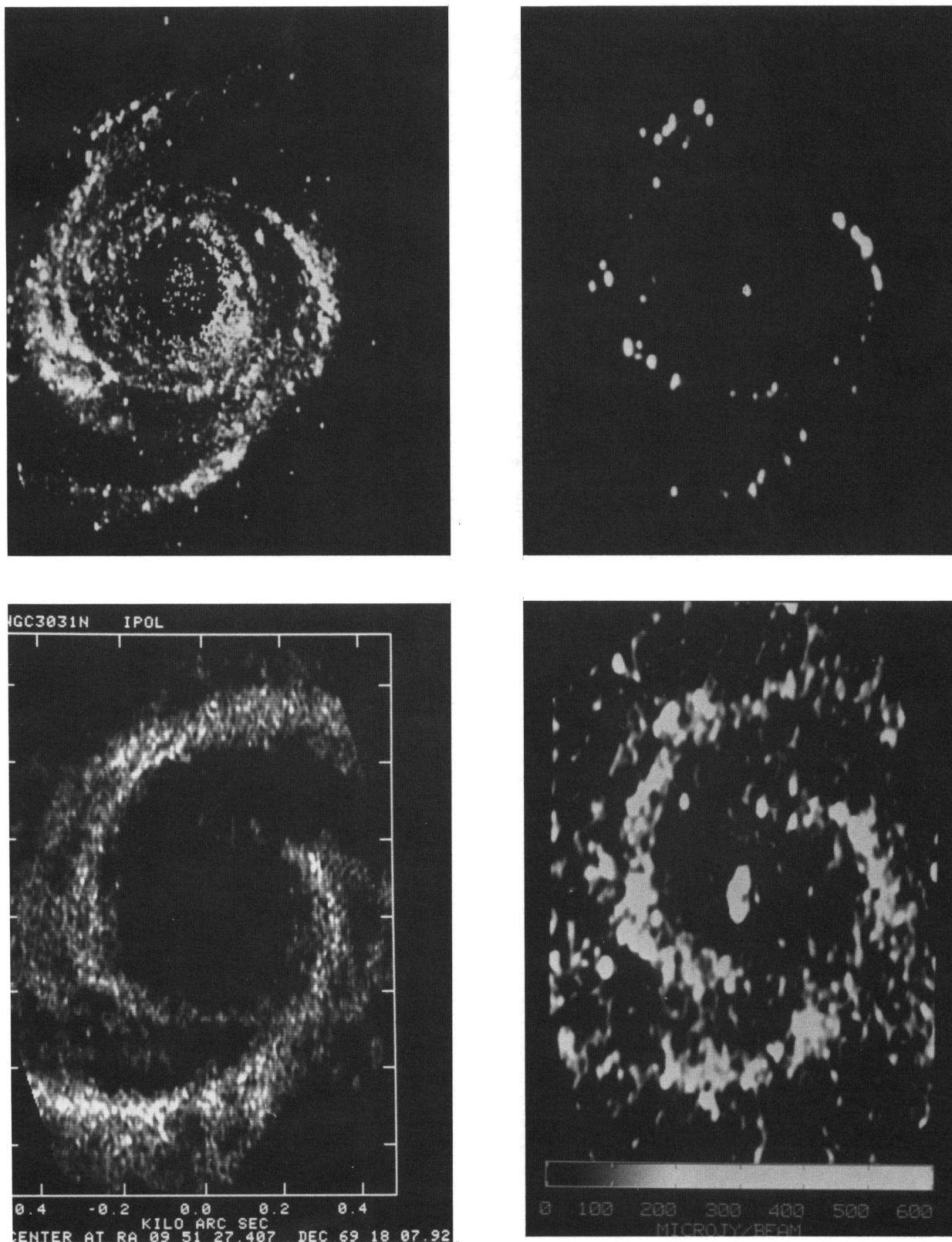
PLATE 7

FIG. 1.—Face-on images of M81: *bottom right panel*, the $\lambda = 20$ cm continuum emission; *bottom left panel*, the H I surface density; *top right panel*, the giant radio H II regions; *top left panel*, the younger stars. All four pictures have the same scale, and the major axis is horizontal.

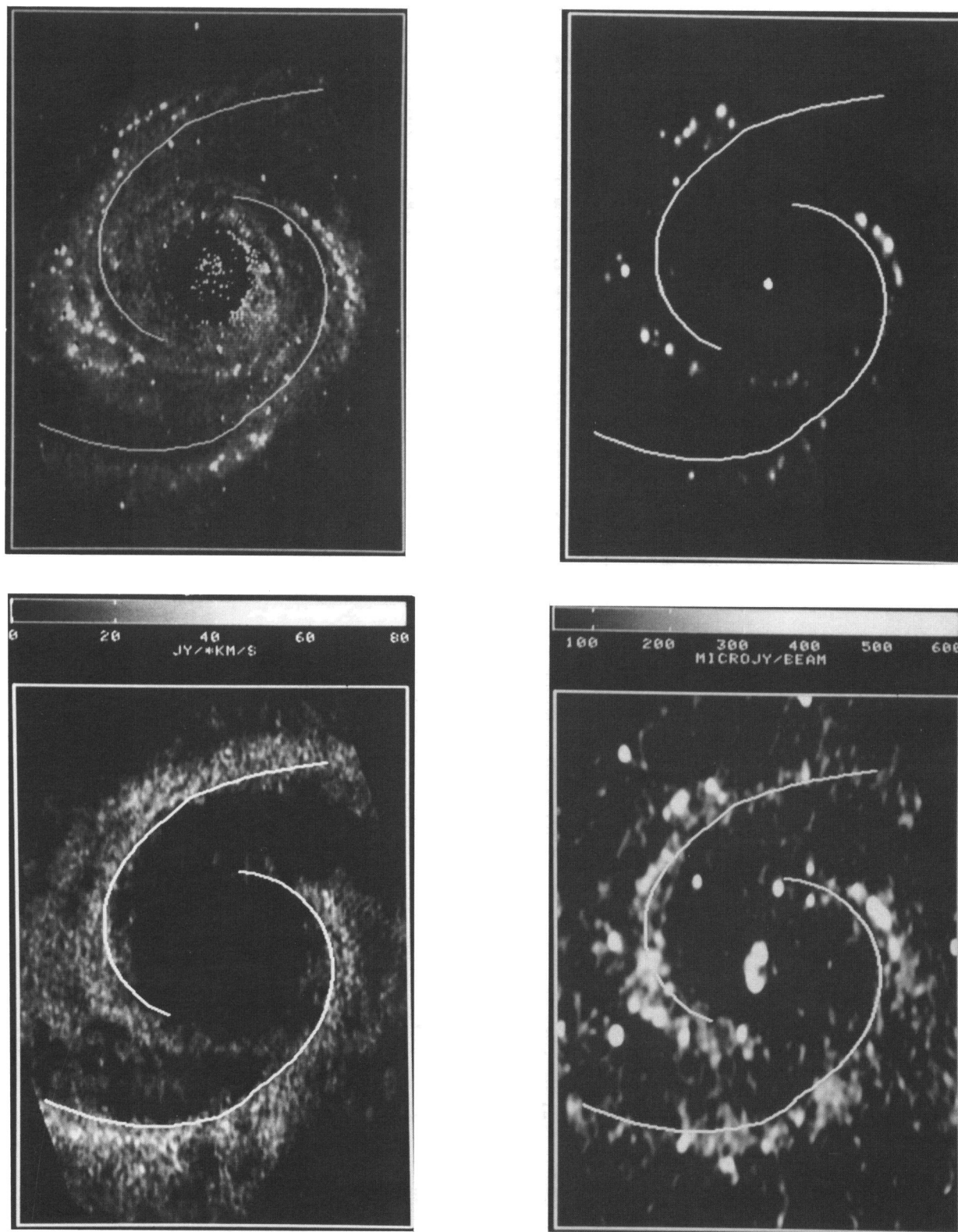KAUFMAN *et al.* (*see* **345**, 676)

PLATE 8

Fig. 2.—Same set of images as in Fig. 1, but with spiral curves added to mark the position of the velocity shock front in the H I gas. Ignore the intensity scale on the H I image.
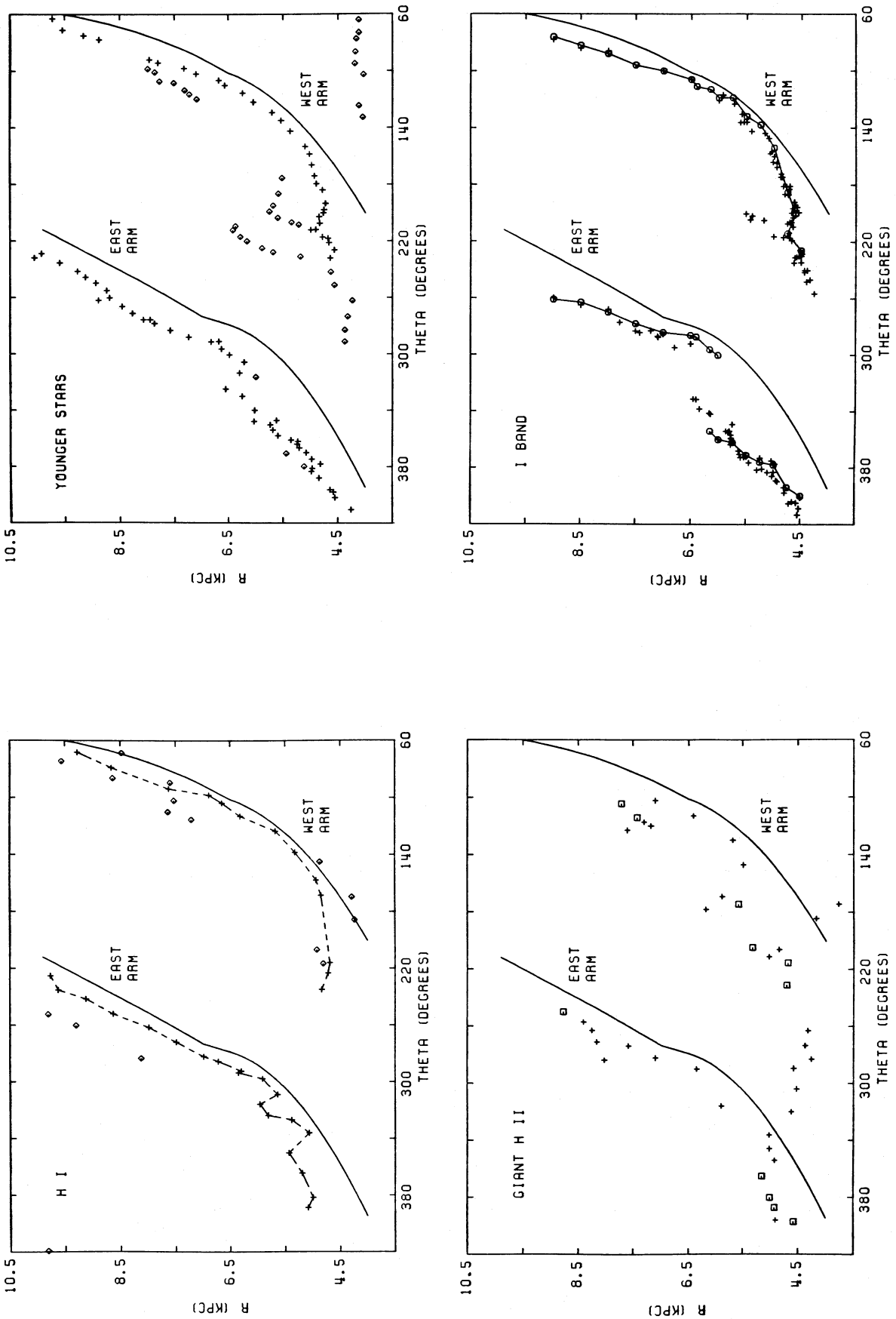
Kaufman et al. (see 345, 676)

FIG. 3.—(a) Positions in face-on polar coordinates of the velocity shock front (solid curve), the ridges of peak H I surface density, and the giant radio H II regions. The major axis is located at $\theta = 180°$ and 360°, and downstream is in the direction of increasing θ. In the graph labeled "H I," the dashed line connecting the plus (+) signs is the main continuous H I ridge along the arm, while the diamonds represent other H I maxima (spurs). In the graph labeled "giant H II," the supergiant H II regions are denoted by open squares; the giant radio H II regions of lower luminosity, by plus (+) signs. (b) Positions in face-on polar coordinates of the velocity shock front (solid curve), the ridges of peak surface brightness on the younger stars image, and the ridges of peak surface brightness on the I-band image, and the gravitational potential minimum on the arms. In the graph labeled "younger stars," the plus (+) signs denote the main continuous ridge of younger stars along the spiral arms, while the diamonds represent other maxima in the younger stars' image, such as spurs and the inner ring. In the graph labeled "I band," the plus (+) signs denote the positions of peak surface brightness on the I-band image, while the lines connecting the open octagons represent the potential minimum. (c) Positions in face-on polar coordinates of the dust lanes (denoted by various symbols) and the velocity shock front (denoted by the solid curve).
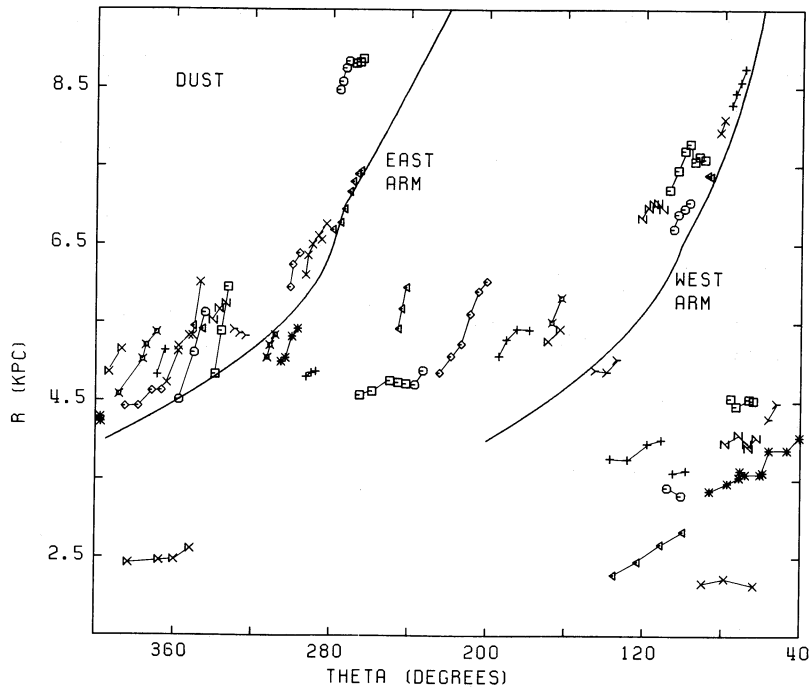
677

FIG. 3c

the ILR. Figure 4 shows that six of the 42 giant radio H II regions lie along the narrow H I ring. Indeed, the H I ring forms the inner boundary to the radial distribution of giant radio H II regions. Furthermore, the younger stars image in Figures 1 and 2 reveals that the stellar arms also emerge from a partial ring (see also the false-color display in Kaufman 1987). Positions measured along the ring in the younger stars image are included in Figure 3b. The partial stellar ring has the same radius as the H I ring. Bash and Kaufman (1986) note that the $\lambda = 20$ cm radio continuum arms end at the H I ring. This can be seen by comparing the respective images in Figures 1 and 2. All this evidence supports the suggestion that the H I ring represents the ILR. Then from the rotation curve adopted by Visser (1980a), the pattern speed Ω_p becomes 15 km s^{-1} kpc^{-1}, and corotation is at 12.5 kpc. Since Visser (1978) interprets the prominent dust lanes at $R = 2$–4 kpc to be part of the same spiral structure as the main spiral arms, he sets the ILR at 2.5 kpc and takes Ω_p equal to 18 km s^{-1} kpc^{-1}. But we believe the bulk of the evidence favors placing the ILR near 4 kpc.

d) The Shapes of the Spiral Arms

In spiral density wave theory, the gravitational potential minimum on the spiral arms is approximately a logarithmic spiral; the theory permits some variation of the pitch angle p with radial distance R (see Visser 1980a). The observed pitch angles in M81 are not constant along the spiral arms. This is pointed out by Oort (1974) for the optical arms, by Hine (1984) for the spiral shock front, and by Bash and Kaufman (1986) for the radio continuum arms. Comparing the shapes of the spiral arms defined by the various tracers in Figure 3, we find the following general features. (1) Except between $R = 6$ and 7 kpc, the local pitch angle of the shock front tends to vary slowly with R. (2) The spiral arms show local deviations from a logarithmic spiral, and some of the distortions differ for different spiral tracers. Bash and Kaufman (1986) suggest that some local distortions may result from the kinetic energy input of

past supernova explosions. This would affect the gas more than the stellar arms and may have produced the kinks in the H I ridge on the eastern arm at $R < 6$ kpc. (3) For all the spiral tracers except some of the dust lanes, the pitch of the western arm flattens substantially at small values of R as the arm goes in to join the H I ring. (4) For most of the spiral tracers, the eastern arm exhibits a large change in pitch angle between $R = 6$ and 7 kpc.

e) The Gravitational Potential Minimum

Smooth, near-infrared arms consist primarily of stars of intermediate age and older, and thus reveal the location of the gravitational potential minimum, since OB stars and M supergiants should appear as bright knots. The spiral arms on the *I* plate of M81 have a smoother appearance than those on the *B* plate. This can be seen from the halftone prints in Elmegreen (1981). The presence of a spiral pattern in the old disk population was first shown in the work of Schweizer (1976) for M81 and by Zwicky (1955) for M51. In the context of the density wave theory, the smooth spiral arms on the *I*-band plate are the response of the old disk stars to the density wave. The response is smooth because the old disk stars are a pressureless gas and no shock waves are produced. Since the young stars (OB stars, M supergiants) have formed recently from the gas, they tend to show the response of the gas in the disk to the density wave. Unlike the stars, the gas may respond very nonlinearly to the density wave and may undergo a spiral shock, as is detected in the H I velocity data on M81.

Elmegreen and Elmegreen (1984) use the *B* and *I* plates to measure the amplitude of the underlying stellar density peak in the spiral arms. They find that in M81 the arm-to-disk contrast (peak-to-trough) in surface mass density increases from a value of 1.5 at $R = 5$–6 kpc to a value of 3 near 8.5 kpc.

To determine the location of the gravitational potential minimum on the spiral arms, we proceeded as follows. We removed the contribution of young stars to the *I*-band image
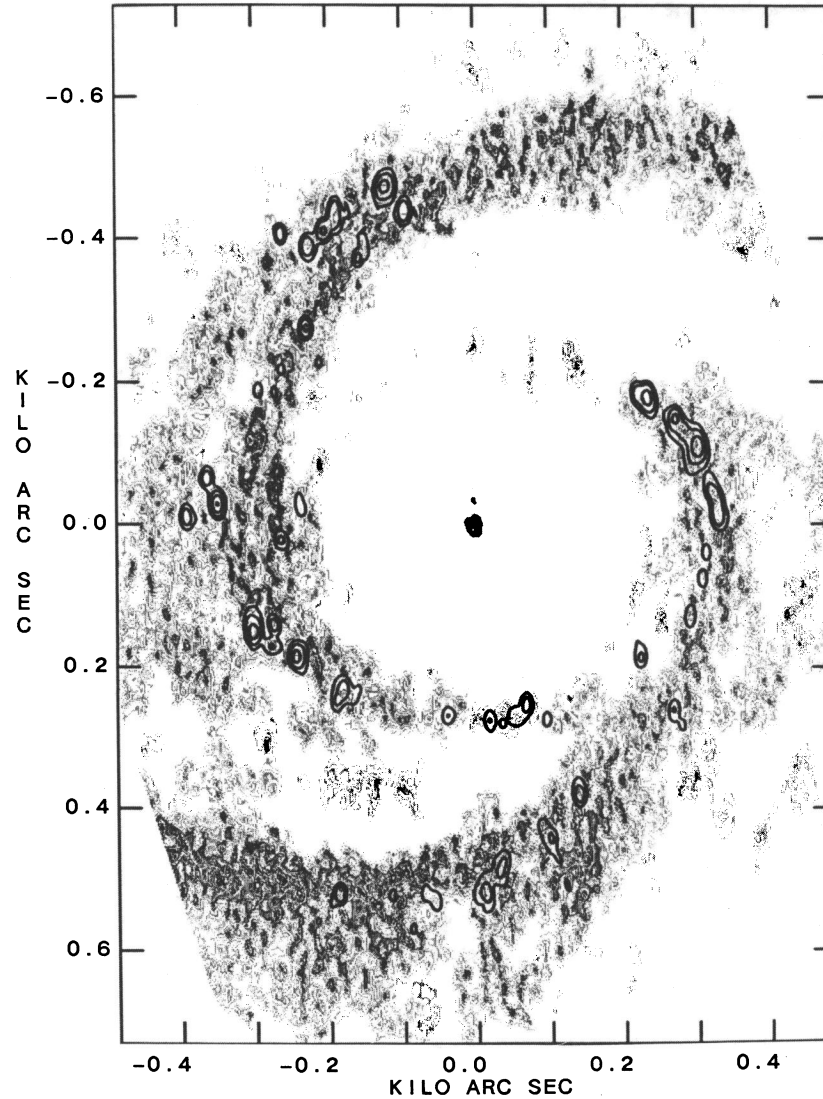
FIG. 4.—Gray-scale display of the face-on H I surface density map. The superposed contours show the locations of the giant radio H II regions. The orientation is the same as in Fig. 1; i.e., the major axis is horizontal and the eastern arm is on the right.

by subtracting a suitable fixed percentage c of the B-band surface brightness from the I-band surface brightness to produce a corrected image $I - cB$. To estimate the appropriate value of c, we adopt the simple extinction-free model by Elmegreen and Elmegreen (1984). Their model assumes (1) a young and an old stellar population (denoted by the subscripts y and o) in the arms, (2) only an old stellar population in the interarm region, (3) a surface mass density of old stars equal to σ_0 in the interarm region and $K\sigma_0$ in the arms, and (4) a surface mass density of young stars equal to σ_y in the arms. Then the B and I intensities in the arm and interarm regions (subscripts a and i) are

$$B_i = (L_B/M)_0 \, \sigma_0 \, ,$$
$$I_i = (L_I/M)_0 \, \sigma_0 \, ,$$
$$B_a = (L_B/M)_0 \, K\sigma_0 + (L_B/M)_y \, \sigma_y \, ,$$
$$I_a = (L_I/M)_0 \, K\sigma_0 + (L_I/M)_y \, \sigma_y \, , \quad (1)$$

where L/M is the luminosity-to-mass ratio, which is assumed

constant for each population all over the galaxy. We wish to solve for the value of c so that in the new image $I' = I - cB$, the surface mass enhancement in the arms will be

$$K = \frac{I'_a}{I'_i} = \frac{I_a - cB_a}{I_i - cB_i} \, . \quad (2)$$

From equations (1) and (2) we obtain

$$c = \frac{I_i}{B_i} \left(\frac{L_I}{L_B}\right)_y \left(\frac{L_B}{L_I}\right)_0 \, , \quad (3)$$

or, using the values for the population luminosity ratios given in Elmegreen and Elmegreen,

$$c = 0.25 \, \frac{I_i}{B_i} \, . \quad (4)$$

Since azimuthal profiles indicated that the value of the surface brightness ratio I_i/B_i at the interarm minima is nearly constant, we used a constant value of c for the entire image.

Figure 5 compares an azimuthal plot of the *I*-band image at $R = 7.5$ kpc with an azimuthal plot of the $I - cB$ image at the same radius. The subtraction makes the waveform closer to sinusoidal in shape. The profiles still tend to be somewhat flat-bottomed because the fainter interarm regions on the *I*-band plate are not much above the sky brightness. Clearly the stellar density wave is not as nonlinear as the original *I*-band azimuthal plots in Elmegreen and Elmegreen (1984) may seem to suggest.

Lubow, Balbus, and Cowie (1986) compute examples where the gas self-gravity in the Milky Way has an important influence on the density wave. However, the following observations suggest that the gas gravity probably has little effect on the location of the gravitational potential minimum in M81. First of all, when averaged over an annulus, the ratio of the H I surface density measured by Rots (1975) to the total mass surface density, taken from the exponential disk model of Visser (1980), ranges from 1% at 5 kpc to 3% at 8 kpc. We argue below that most of the interstellar gas is in the form of H I. According to Lubow *et al.*, the gas self-gravity is unimportant if the gas content is less than $\sim 3\%$. Second, the measured amplitude of the stellar surface density perturbation in the arms of M81 is ~ 4 times the amplitude of the H I surface density perturbation. Using the surface mass enhancement K (from Elmegreen and Elmegreen) and the exponential disk model of Visser, we find that over the range $R = 5$–8 kpc, the amplitude of the stellar perturbation is 40–60 $M_\odot$ pc^{-2}. The H I shock is resolved in the VLA data, and the amplitude of the H I perturbation in the same range of R is only 10–15 $M_\odot$

pc^{-2}. Therefore we assume that the local gravitational potential minimum on the arms of M81 occurs at the stellar density maximum.

Thus we identify the maxima on the azimuthal plots of the $I - cB$ image with the potential minimum. These positions, shown in Figure 3*b*, are measured to an average accuracy of $\pm 3°$ in θ. While the separation between the potential minimum measured on the $I - cB$ image and the surface brightness ridge on the original *I*-band plate is small, the potential minimum is usually a little closer to the shock front. Except in the range $R = 4.8$–6 kpc, the stellar arms are separated by $\sim 180°$ in azimuth, as expected for a symmetric $m = 2$ mode. The 4.8–6 kpc range includes the northern portion of the western arm, so tidal perturbations by M82 may have played a role here, as M82 is just north of M81.

Usually the results of theoretical density wave calculations are presented in terms of the spiral phase angle η. Figure 6 shows the positions of the various spiral tracers in η versus R coordinates, where

$$\eta = \frac{2}{\tan p(R_s)} \ln \left(\frac{R}{R_0} \right) + 2\theta , \qquad (5)$$

R_0 is the radius where the $\eta = 0$ spiral crosses the major axis, and p is the local pitch angle of the shock front. The subscript s indicates the shock front, and we choose $\eta_s = 0$ for the eastern arm and $\eta_s = 2\pi$ for the western arm. The spiral phase angle η increases in the downstream direction. The displacement of the potential minimum downstream from the shock front is
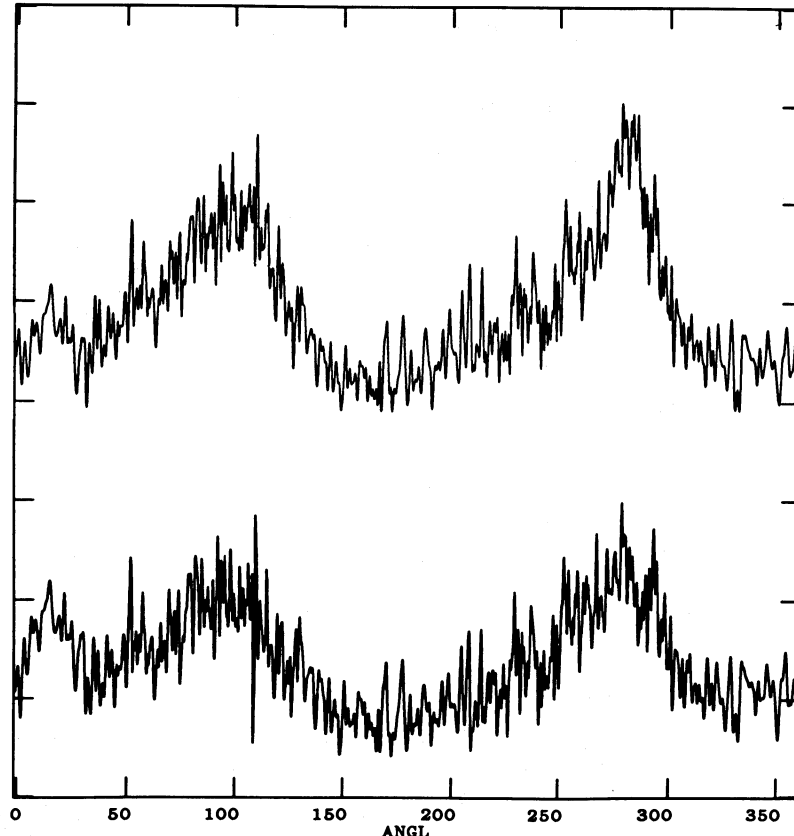

FIG. 5.—Azimuthal surface brightness plots at galactocentric radius $R = 7.5$ kpc of the *I*-band image (*light line*) and of the $I - cB$ image (*heavy line*)

$\delta\eta_M = \eta - \eta_s$. Obviously, positions in the inner part of M81, where there is no spiral shock, do not appear in Figure 6. In particular, the inner ring (identified by us as the inner Lindblad resonance) does not appear in Figure 6.

For the western arm, the situation is simple: the H I ridge coincides with the potential minimum (see Fig. 6b) and the ridge of the younger stars either coincides with the potential minimum or lies just marginally downstream from it (see Fig. 6a). Thus, after the H I gas passes the shock front on the western arm, its velocity component u_η perpendicular to the arm continues to decrease until the gas reaches maximum compression at the potential minimum. Over the range $R = 5$–9 kpc on the western arm, the potential minimum is displaced downstream from the velocity shock front by $\delta\eta_M = 8°$–28°, or equivalently, by 4°–13° in azimuth (see Fig. 3b). The uncertainty in $\delta\eta_M$ is $\pm 9°$, mainly from the uncertainty in the shock position. For $R < 5$ kpc on the western arm, $\delta\eta_M$ increases to values as large as $\cong 100°$. Comparison with the predictions of Visser's (1980b) model will be made below.

On the eastern arm, the H I ridge lies upstream from the potential minimum, except for $R = 6$–7.5 kpc where the two coincide (see Fig. 6b). Figure 6a shows that the younger stars ridge on the eastern arm lies near the potential minimum but is sometimes upstream, sometimes downstream from the potential minimum. For the eastern arm, the displacement $\delta\eta_M$ of

the potential minimum from the velocity shock front equals 18°–55° for $R = 6.2$–9 kpc but takes values of 100°–175° for $R < 6.2$ kpc. For both arms, the observed values of $\delta\eta_M$ at small values of R are much greater than the values predicted by Visser's (1980b) hydrodynamic model. In his final model of M81, $\delta\eta_M$ equals 10° for $R = 3$–6 kpc and then increases monotonically to 28° at $R = 8$ kpc. The discrepancy at small values of R may be mainly the result of his setting the ILR at 2.5 kpc instead of 4 kpc.

In linear distance, the displacement of the H I ridge from the shock front is about the same ($\cong 500$ pc) in both arms. Figure 7 exhibits the displacements of the spiral tracers in terms of the perpendicular distance d from the spiral shock front, where we use the approximation

$$d = (R - R_s) \cos p(R_s) , \qquad (6)$$

with R_s the radial distance of the shock front at the same azimuth θ as the object. The perpendicular displacement d is positive in the downstream direction.

To account for the downstream displacement of the H I ridge from the spiral shock front in M83, Allen, Atherton, and Tilanus (1986) suggest that the interstellar gas is primarily molecular until dissociated in the neighborhood of the giant H II region complexes. Although this explanation may be correct for the strong CO galaxies such as M51 and M83, it
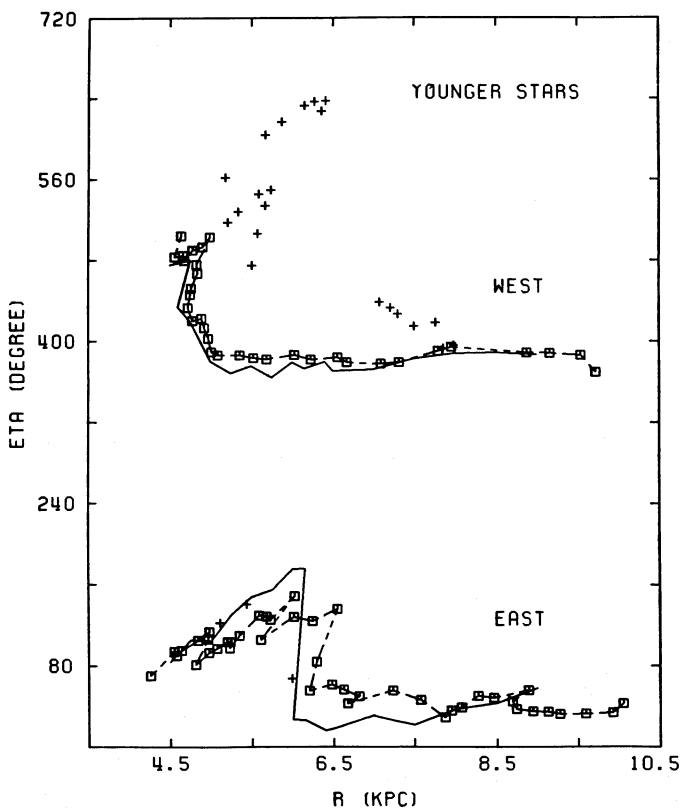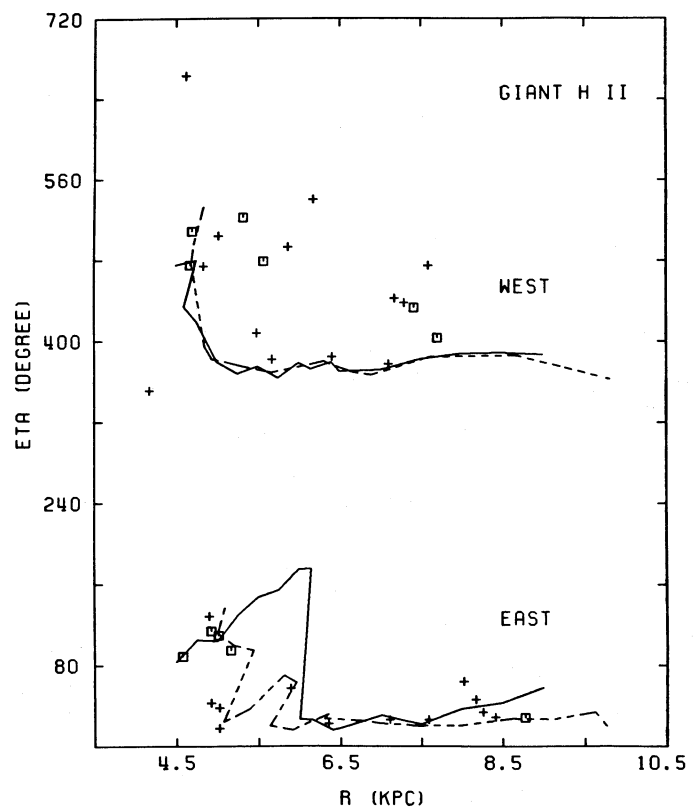

FIG. 6a

FIG. 6b

FIG. 6.—(a) Spiral phase angle η vs. R for the younger stars. Open squares connected by a dashed line represent the main ridge of younger stars along the arm. Spurs are denoted by plus (+) signs. Solid curve represents the gravitational potential minimum. The H I velocity shock front is located at $\eta = 0°$ (eastern arm) and 360° (western arm). The spiral phase increases in the downstream direction. The uncertainty in η equals $\pm 8°$ to $\pm 9°$ for the younger stars and $\pm 9°$ for the potential minimum. (b) Spiral phase angle η vs. R for the giant radio H II regions. The supergiant H II regions are denoted by open squares, the giant H II regions by plus (+) signs. Solid curve represents the gravitational potential minimum, and dashed curve is the main ridge of peak H I surface density along the arm. The uncertainty in η equals $\pm 7°$ to $\pm 8°$ for the H II regions and the H I ridge.
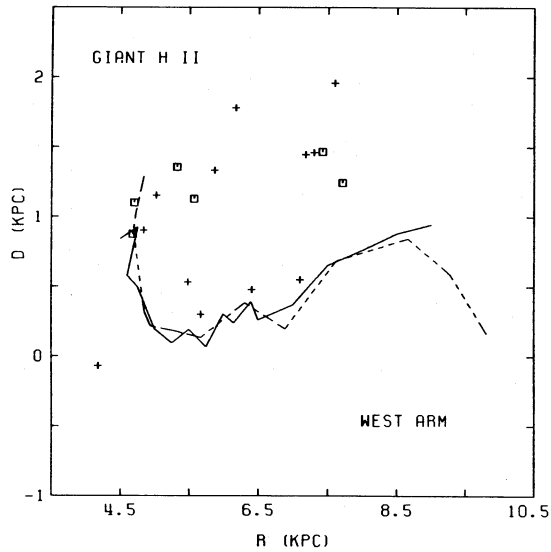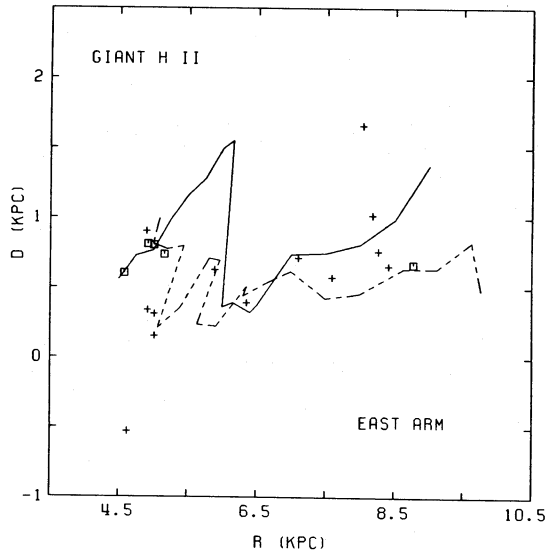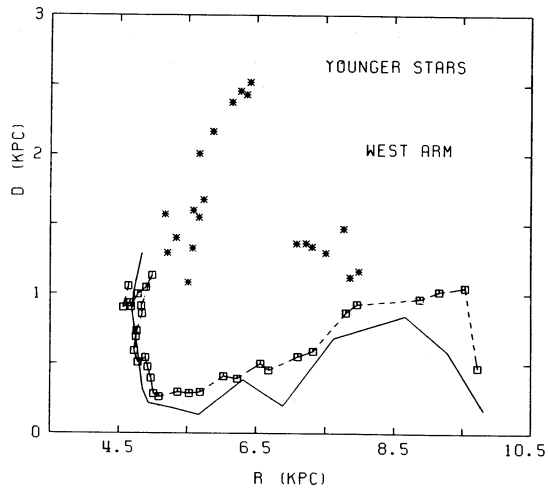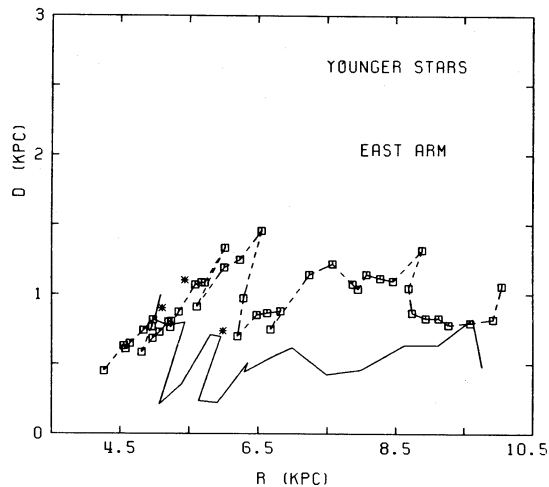
FIG. 7*a*

FIG. 7*b*

FIG. 7*c*

FIG. 7*d*

FIG. 7.—(*a*)–(*b*) The perpendicular displacement *d* of the giant radio H II regions from the spiral shock front in the H I gas. Symbols and curves have the same meaning as in Fig. 6*b*. The perpendicular distance *d* is positive in the downstream direction. For the H II regions and the H I ridge, the uncertainty in *d* varies from ± 0.07 kpc at $R = 5$ kpc to ± 0.17 kpc (*eastern arm*) or ± 0.20 kpc (*western arm*) at $R = 8$ kpc. For the potential minimum, the uncertainty in *d* varies from ± 0.08 kpc at $R = 5$ kpc to ± 0.20 kpc (*eastern arm*) or ± 0.22 kpc (*western arm*) at $R = 8$ kpc. (*c*)–(*d*) The perpendicular displacement *d* of the younger stars from the spiral shock front. Open squares connected by a dashed line represent the main younger stars ridge along the arm. Spurs are denoted by asterisks. Solid curve represents the main ridge of peak H I surface density. For the younger stars' ridge, the uncertainty in *d* varies from ± 0.08 kpc at $R = 5$ kpc to ± 0.18 kpc (*eastern arm*) or ± 0.21 kpc (*western arm*) at $R = 8$ kpc.

does not seem to apply to M81. The CO emission from M81 is very weak (Brouillet, Baudry, and Combes 1988). Also, according to Figure 3*c* and the detailed study of the dust lanes by Kaufman, Elmegreen, and Bash (1989), there is no prominent, long, molecular dust lane at the velocity shock front in M81. And in § VII below, we find that the cross-arm distribution of extinction sampled by the giant radio H II regions shows no tendency for $A_v/N(\text{H I})$ to be greater closer to the shock front. Here $N(\text{H I})$ is the column density of H I. In the absence of evidence for a major lane of molecular gas upstream from the H I ridge, the H I ridge cannot result from the dissociation of such a molecular component. The H I ridge is produced simply by compression of the upstream atomic hydrogen.

Instead we view the 500 pc displacement of the H I ridge from the shock front in M81 as the shock thickness. The set of

surface density profiles in Hine (1984) shows that the observed gradient in H I surface density at the inside edge of the arm is much less steep than predicted by Visser's (1980*a*, *b*) fluid model. Hine stresses that the arm widths derived from the VLA H I data on M81 agree well with those in the cloudy density wave model by Roberts and Hausman (1984) for the Milky Way. Roberts and Hausman predict a width of 300–600 pc for the "shock front," comparable to what we observe here. The fact that the observed displacement of the H I ridge from the shock front is approximately the same for both arms suggests that the mean free path for H I clouds entering the arm is roughly the same for the two arms. Alternatively, Roberts and coworkers conclude that the thickness of the "shock front" in their cloudy model results from orbit crowding of large clouds and is independent of the cloud mean free path.

There are indications in Figure 7 that some of the structure in the younger stars ridge line may correspond to kinks in the H I ridge line if the latter were displaced suitably downstream. Since the young stars are recently formed from the gas, they reflect the response of the gas to density waves and to other sources of shock waves, such as past supernova explosions.

IV. THE LOCATIONS OF THE GIANT RADIO H II REGIONS

The set of giant radio H II regions displayed in Figure 1 clearly defines two spiral arms and part of the inner ring. With one exception, all of these H II regions lie on either the broad H I arms or the H I ring (see Fig. 4). If the inner ring sources are omitted, then nearly all the giant radio H II regions are downstream from the spiral shock front (see Figs. 3, 6, and 7).

The observed cross-arm distribution of giant radio H II regions conflicts with the predictions of the ballistic particle model of Leisawitz and Bash (1982) for M81. The observed set of giant radio H II regions is spread out across a zone 1.0–1.5 kpc wide, with 75% of the regions at perpendicular distances $d = 0.5$–1.5 kpc from the shock front. In contrast, their model predicts that all the H II regions associated with the spiral arms should be located in one of the following two types of clumps: (a) at all values of R_s there should be a clump of H II regions very close to or just upstream from the spiral shock front, and (b) at small values of R_s (e.g., near where the arms cross the major axis), there should be another clump of H II regions extending farther downstream. The first type of clump is essentially missing in the data. The discrepancy is particularly severe at large values of R_s, where the model predicts that all giant H II regions should lie very near the spiral shock or just upstream from it, while the observed giant radio H II regions are 0.5–2.0 kpc downstream from the shock front.

Kaufman et al. (1987) discuss the radial distribution of the set of giant radio H II regions in terms of the number of H II regions per annulus. They suggest that the radial distribution predicted by the Leisawitz-Bash model may be adjusted to fit the observed radial distribution by (1) shifting the location of the ILR to the position of the inner H I ring and by (2) changing the adopted radial distribution of small clouds or GMC birthsites. However, the cross-arm distribution shown in Figure 7 provides a more stringent test of this model.

The discrepancy between the predicted and observed cross-arm distributions of giant H II regions leads us to question the assumptions Leisawitz and Bash make about the velocities and the birthplaces of the giant clouds in which the giant H II regions form. They assume that the giant clouds are launched from the shock front at velocities close to the postshock velocity in Visser's (1980a, b) fluid model. We consider the following three parameters in their ballistic particle model as possible sources of the above discrepancy: (a) the location of the ILR, (b) the launch velocities, and (c) the launch site. In § III we argued that the ILR is at 4 kpc, the position of the inner H I ring, rather than at the 2.5 kpc value adopted by Leisawitz and Bash (following Visser). This shifts the location of the maximum in the predicted radial distribution of giant H II regions (see Kaufman et al. 1987), but the main effect on the predicted cross-arm distribution of the set of giant H II regions would result from the corresponding 3 km s^{-1} kpc^{-1} decrease in the pattern speed. We checked that near the minor and major axes the mean pre and postshock velocities measured from the VLA H I data agree with the predictions of Visser's model. Using the new choice of pattern speed, we recomputed the orbits of ballistic particles launched with exactly the post-
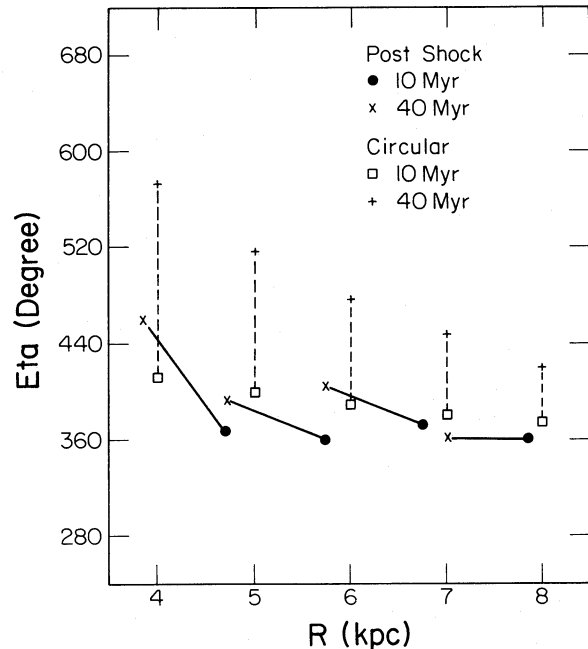

FIG. 8.—Comparison of the predicted phase angle displacements of ballistic particles launched from the spiral shock at the postshock velocity with those of particles launched at the circular velocity. The shock front is at $\eta = 360°$. The indicated time values represent the elapsed time since leaving the shock front.

shock velocities of Visser's model. Figure 8 shows the resulting values of the spiral phase η at two values of the elapsed time t since leaving the shock front. The change in the choice of pattern speed makes little difference in the orbits relative to those shown by Leisawitz and Bash. In contrast to particles traveling on circular orbits, the particles launched at the postshock velocity move inward, toward the center of the galaxy, on orbits that go only slightly downstream from the spiral shock front during the first 40 million yr. If we compare Figure 8 with Figure 6b, we see that for reasonable values of t the particles launched at postshock velocities do not cover the range of η filled by the giant radio H II regions. Indeed, initial velocities that are approximately circular would seem to do a better job of reproducing the observed distribution. Thus, if the choice of launch velocity is the main problem, then the clouds which produce massive OB associations do not leave the shock front with the same velocities as the mean motion of the H I gas.

However, in § III we point out that the observed shock width is ~500 pc. This is not the same as the very narrow shock front assumed for the launch site in the Leisawitz-Bash model. According to Figure 3c and the study of the dust lanes by Kaufman, Elmegreen, and Bash (1989), there is no prominent long dust lane with high extinction at the velocity shock front. Thus, the notion of a dust lane that breaks up into GMCs at a narrow spiral shock front does not seem to apply to M81. Therefore we feel that the problem with the Leisawitz-Bash model is first the choice of launch site; this necessarily affects the launch velocities.

On the other hand, in the cloudy model by Roberts and coworkers, new stellar associations tend to form where the clouds congregate, i.e., near the potential minimum, and then travel downstream initially. In one example described by Hausman and Roberts (1984), more than half of the collisionally triggered stellar associations are born within
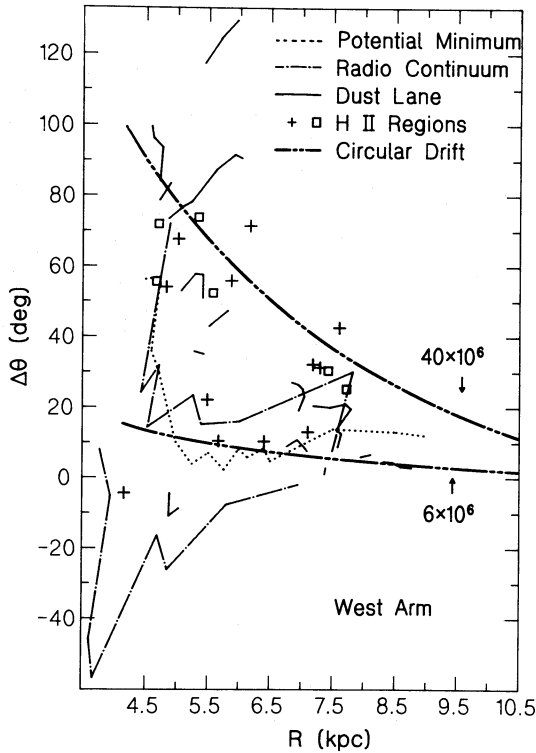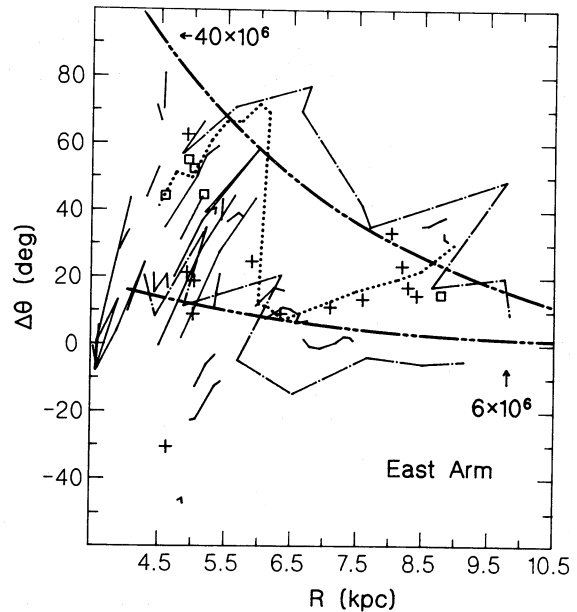
FIG. 9.—(*a*) The azimuthal displacements, $\Delta\theta = \theta - \theta_s$, from the velocity shock front of various spiral tracers on the western arm. The value of $\Delta\theta$ is positive in the downstream direction. Curves for the radio continuum emission mark the approximate half-power positions of the nonthermal radio emission. Supergiant H II regions are denoted by open squares; giant radio H II regions of lower luminosity by plus signs. For clarity, the ridge lines for H I and for the younger stars are omitted because they lie close to the potential minimum. For material traveling at the local circular velocity, the labels on the circular drift curves indicate the time interval in years since passing the shock front. (*b*) Same as (*a*), but for the eastern arm.

$\Delta\eta = \pm 30°$ of the potential minimum. When self-gravity is included, Roberts, Adler, and Stewart (1988) report that the peak of the predicted distribution of young stellar associations occurs a few hundred parsecs downstream from the ridge of maximum density. We compare these predictions with our data but caution that their models were calculated for density wave parameters more appropriate to the Milky Way than to M81. The near coincidence between the potential minimum and the younger stars ridge line in M81 (see Fig. 6) is consistent with their models. We find that 55% of the giant radio H II regions in M81 lie within $\Delta\eta = \pm 30°$ of the potential minimum, another 15% lie upstream, and 30% lie downstream from that range. On the eastern arm, more than half of the H II regions congregate on the H I ridge. Thus the cloudy model by Roberts and coworkers seems to be more successful than the model by Leisawitz and Bash in fitting the observed cross-arm distribution of the set of giant radio H II regions.

We conclude that the observed cross-arm distribution of giant radio H II regions is consistent with the notion that orbit crowding near the potential minimum plays an important role in producing the massive OB associations in the spiral arms.

The set of giant radio H II regions includes 11 supergiant H II regions (i.e., regions with excitation parameters $U > 230$ pc cm^{-2}). Figures 3, 6, and 7 show that the supergiant H II regions tend to be farther downstream from the shock front than the rest of the set. The temptation is to conclude that it takes more time to form the luminous H II regions. In Figure 9 we compare the values of the azimuthal displacement $\Delta\theta = \theta - \theta_s$ from the shock front of various tracers. The displacement $\Delta\theta$ is positive

in the downstream direction. If the clouds and the stars were to travel on circular orbits at the local circular velocity, then the azimuthal displacement from the shock front after a time interval t would be given by $\Delta\theta = (\Omega - \Omega_p)t$. Figure 9 shows that the circular drift curves corresponding to $t = 6 \times 10^6$ and 40×10^6 yr roughly bound the observed distribution of giant radio H II regions. However, in general, we expect ballistic particles to travel on epicyclic, not on circular orbits. In fact, Roberts and Stewart (1987) note that some particles in their simulations undergo episodes of temporary retrograde motions in the arms; consequently, an older H II region is not necessarily farther from the shock front.

Some of the steps leading to the formation of massive OB associations are different in a galaxy like M81 where most of the hydrogen is in atomic form than in M51, where the hydrogen is primarily in molecular form. For example, from high-resolution CO observations, Vogel, Kulkarni, and Scoville (1988) suggest that large OB associations in M51 are produced after giant molecular associations near the spiral shock front break up into GMCs. The displacements of the giant H II regions from the spiral shock front in different galaxies may depend on whether most of the gas at the spiral shock is molecular or atomic. The Leisawitz-Bash model may be more appropriate to a galaxy with a narrow shock front and a high molecular content, such as M51, than to M81.

V. THE NONTHERMAL RADIO ARMS

Bash and Kaufman (1986) find that the nonthermal radio arms in M81 are patchy and have a characteristic width of 1–2 kpc, too broad for the emission to come from just the shock

front in Visser's (1980a, b) fluid model. Except near the northern major axis, where some emission is upstream from the shock, the radio continuum arm begins near the spiral shock front and extends appreciably downstream (see Fig. 2). To study the extended emission from the arms, Bash and Kaufman (1986) made 26 intensity profiles across the radio continuum arms at positions that avoid the giant radio H II regions. From the profiles, we determine the approximate half-power points of the nonthermal emission. These are shown in Figure 9. The half-power width of the nonthermal arm refers to the excess above the axisymmetric disk. Since the arm profiles are non-Gaussian, the half-power points are eyeball estimates only. For $R > 5$ kpc on the western arm, or $R > 6$ kpc on the eastern arm, the radio continuum emission is approximately centered on the potential minimum. The potential minimum lies close to the younger stars ridge line, and, in fact, the radio continuum emission is roughly centered on the younger stars ridge line for $R > 5$ kpc on both arms. Despite the presence of a shock in the H I gas, which might be expected to increase the synchrotron emission via a compression of ambient fields and interstellar gas, the radio continuum profiles show no tendency for the inside edge of the profile to be steeper than the outside edge. For M51, where the signal-to-noise ratio is greater than in the M81 data, Tilanus et al. (1988) report that intensity profiles across the nonthermal radio arms are steeper on the outside than on the inside edge.

The width of the radio continuum arms in M81 is similar to the width of the density enhancement in the cloudy model by Roberts and coworkers. The zone of active star formation along the spiral arms is also where supernova explosions in massive stars accelerate cosmic-ray electrons. Berkhuijsen (1984) concludes that in M31, M33, and the Milky Way galaxy, the nonthermal and free-free flux densities are consistent with an SNR origin for the relativistic electrons. Since the radio arms in M81 are roughly centered on the younger star ridge and are spread out like the stellar arms, the simplest interpretation is that the cosmic-ray electrons in M81 also come from SNRs. This is supported by the evidence presented below.

Figures 9 and 10 show where the set of giant radio H II regions is situated relative to the radio continuum arms (see also the composite false-color picture in Kaufman 1987). The giant radio H II regions tend to congregate near the center of the radio arm or near the outer edge. The width of the radio arm is comparable to or somewhat greater than the width of the arm defined by the distribution of giant radio H II regions. To account for the steep decline in radio emission at the downstream edge of the arm in M51, Allen (1988) postulates that the energy input from active star formation increases the scale height of the gas and thus decreases the magnetic field B and the synchrotron emission. The presence of several giant radio H II regions near the downstream edge of the radio continuum arm in M81 seems consistent with this suggestion. Also, Kaufman, Elmegreen, and Bash (1989) find that in the vicinity of the giant H II regions in M81, there are dust filaments that appear to be clouds 100–200 pc above the midplane. Although the two most luminous H II regions are located near the center of the radio arm, within 100 pc of the potential minimum, even these two H II regions (which are on the eastern arm near $R = 5$ kpc) may have had some local influence on the synchrotron emission, as will be described below. Near the arm center, the compression of the gas at the potential minimum and the enhanced injection of cosmic-ray electrons from the zone of most active star formation both tend to increase the synchro-

tron radiation and thus compete with the decrease in emission caused by the suggested increase of scale height.

The lower resolution radio measurements by Krause, Beck, and Hummel (1987, 1989) provide other evidence for the influence of active star formation on the nonthermal radio emission from M81. Although the synchrotron emission is strongest in the arms, the polarized emission has maximum intensity in the interarm region. Krause, Beck, and Hummel (1989) conclude that the uniform component of the B field decreases in the arms because energy input from OB associations produces more turbulence there. The magnetic field is more regular in M31 than in M81 (see Beck 1986); this may be the consequence simply of more active star formation in M81.

Over the range of R where the giant radio H II regions occur ($R = 4$–9 kpc), 30% of the spiral arm emission "seen" by the VLA at $\lambda = 20$ cm comes from the set of giant radio H II regions. The spiral arm radio emission discussed here represents just the excess from the spiral arms, since the disk of M81 is too extended for the VLA to detect the axisymmetric component. Still, the contribution of the set of giant radio H II regions to the radio spiral arms is surprisingly large.

The range of R where the radio continuum arms are bright is approximately the same as the range of R where the giant radio H II regions occur (see Fig. 10). We compare the distributions along the spiral arms of (1) the $\lambda = 20$ cm flux density $S_\nu(\text{H II})$ from the set of giant radio H II regions and (2) the more extended $\lambda = 20$ cm emission $S_\nu(\text{arm})$ from the spiral arms after the contribution from giant radio H II regions is removed. The flux density $S_\nu(\text{arm})$ is a combination of nonthermal emission plus free-free emission from fainter H II regions and diffuse sources; the spectral index image in Bash and Kaufman (1986) indicates that much of the extended emission from the arms is mildly nonthermal. To obtain $S_\nu(\text{H II})$ we simply summed the flux densities of the H II regions measured by Kaufman et al. (1987). The set of giant radio H II regions dominates the free-free emission from the spiral arms. From observations with the 100 m telescope at Effelsberg, Beck, Klein, and Krause (1985) find that the total integrated flux density of M81 (nucleus omitted) is 170 ± 30 mJy at $\lambda = 6.3$ cm and estimate that $\sim 15\%$ of this is free-free emission. The flux density of the set of giant radio H II regions considered here is equivalent to 15 mJy at $\lambda = 6.3$ cm and thus accounts for $\sim 60\%$ of the estimated total free-free radiation from the galaxy. Whereas the giant radio H II regions in M81 are situated on the spiral arms and the inner ring, the total free-free emission also contains contributions from interarm regions; consequently, the set of giant radio H II regions is responsible for at least 60% of the free-free radiation from the arms.

To measure $S_\nu(\text{arm})$ we transformed the $\lambda = 20$ cm continuum image into polar coordinates and divided each spiral arm into seven boxes. Each box cuts across the arm to include approximately all the spiral arm emission at that value of R, but each of the boxes has the same (ΔR, $R\Delta\theta$) dimensions to make a comparison of the flux densities from each box along the arm meaningful. Figure 11 compares the values of $S_\nu(\text{arm})$ and $S_\nu(\text{H II})$ from these boxes. Note that Kaufman et al. (1987) plot the radial distribution of giant radio H II regions in terms of the flux density per annulus; this should not be confused with Figure 11, which gives the flux density from boxes of fixed area along the arms. Although $S_\nu(\text{arm})$ and $S_\nu(\text{H II})$ both tend to decrease as R increases, the ratio of $S_\nu(\text{H II})$ to $S_\nu(\text{arm})$ varies considerably from box to box. If we compare boxes at the same R on both arms, we notice that in five out of seven cases the
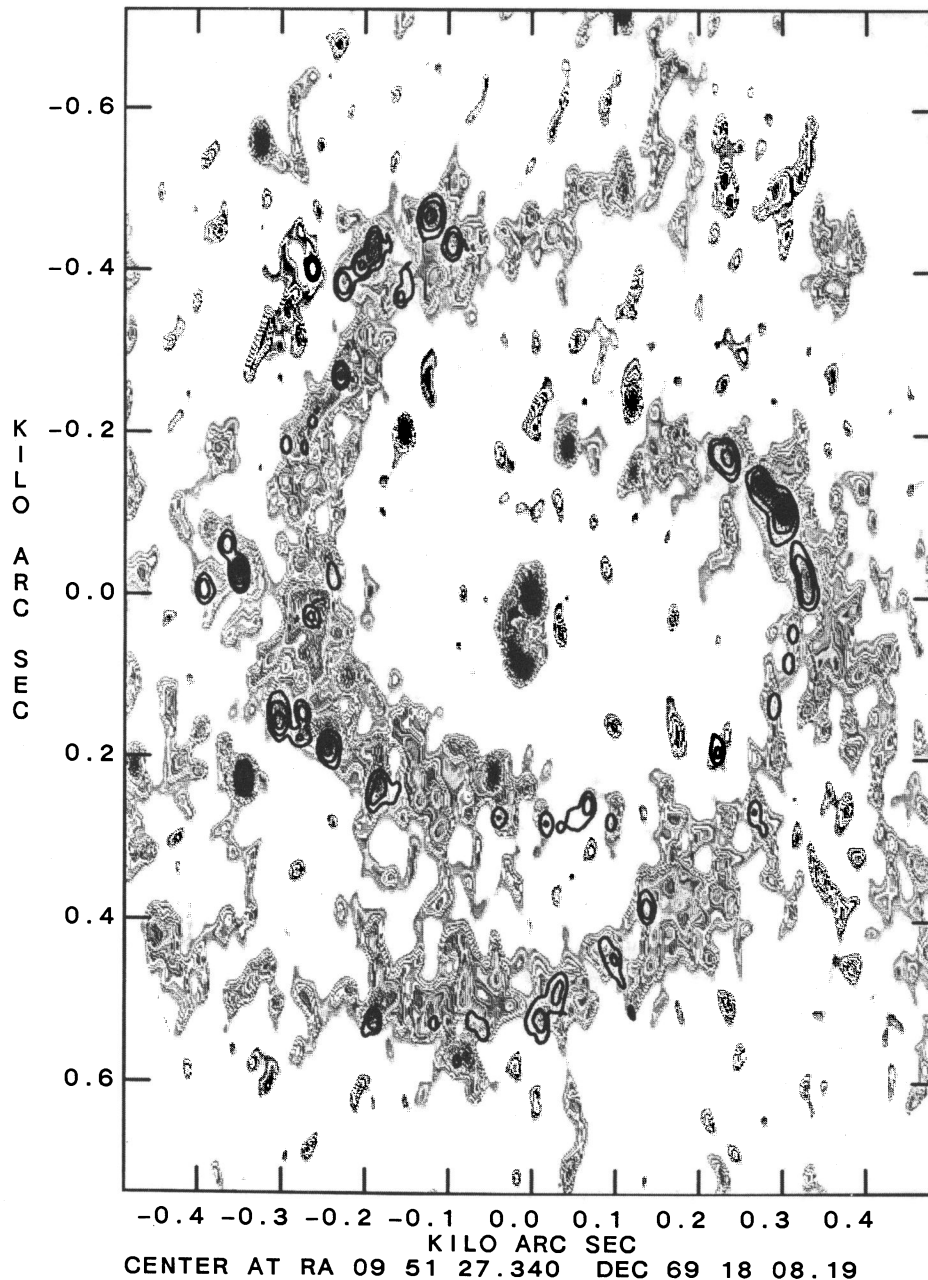
FIG. 10.—Gray-scale display of the face-on $\lambda = 20$ cm continuum image. The superposed contours show the positions of the giant radio H II regions. The orientation is the same as in Fig. 1.

arm with the greater value of $S_\nu(\text{H II})$ has the smaller value of $S_\nu(\text{arm})$. The box containing the two most luminous H II regions occurs on the eastern arm; comparing with the box at the same R on the western arm, we find that $S_\nu^E(\text{arm})/S_\nu^W(\text{arm}) = 0.7$, while $S_\nu^E(\text{H II})/S_\nu^W(\text{H II}) = 2.2$. The anti-correlation is consistent with the suggestion of an increased scale height causing some decrease in the synchrotron emission when the energy input from OB stars is large.

We next determine the arm-to-disk ratio for the radio continuum emission. For this we need to estimate the surface brightness $I_\nu(\text{disk})$ of the axisymmetric disk at $\lambda = 20$ cm. To obtain $I_\nu(\text{disk})$, we adopt the radial distribution of $\lambda = 6.3$ cm continuum emission measured by Beck, Klein, and Krause (1985) with the 100 m Effelsberg telescope and extrapolate to

$\lambda = 20$ cm by using their radial distribution of the $\lambda = 2.8$ to $\lambda = 6.3$ cm spectral index. The $\lambda = 20$ cm flux densities derived by this extrapolation tend to be slightly greater than those measured by Segalovitz (1977) with the Westerbork Synthesis Radio Telescope but have rather large uncertainties because of the uncertainty in spectral index. Then to derive $I_\nu(\text{disk})$, we use the VLA measurements to remove the contributions from the spiral arms and from any discrete background sources. At 20 cm, $I_\nu(\text{disk})$ is roughly constant at 1.0 ± 0.2 mJy kpc^{-2} for $R = 4–7$ kpc and then decreases as R increases (see Fig. 11 for the relative distribution).

Using the set of 26 cross-arm intensity profiles from Bash and Kaufman (1986), we obtain the arm amplitude $I_\nu^a(\text{peak})$ for each slice across the arm on a $\lambda = 20$ cm map that has a linear
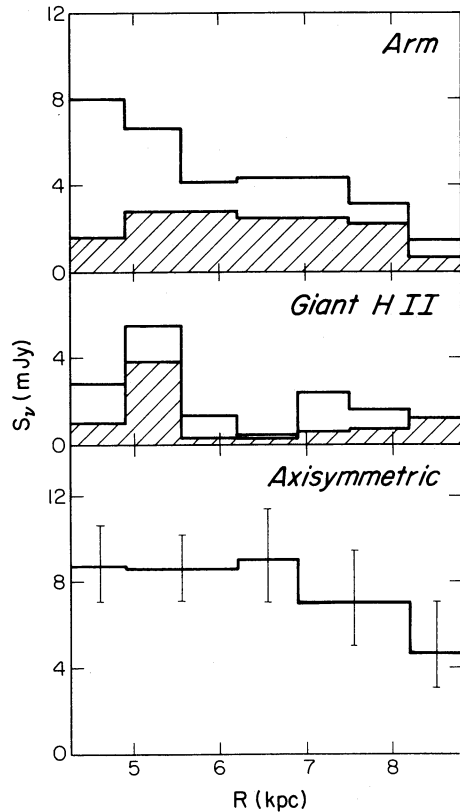
FIG. 11.—Various components of the $\lambda = 20$ cm continuum emission from the spiral arms of M81. The flux density from a series of equal-area boxes along the arms is separated into contributions from (1) the axisymmetric disk, (2) the giant radio H II regions, and (3) the extended arm emission in excess of the disk. (The extended arm emission excludes the giant radio H II regions.) Each box cuts across the spiral arm to include most of the spiral arm emission at that value of R. The hatched regions refer to emission from just the eastern arm. The axisymmetric component is an extrapolation from the $\lambda = 6.3$ cm single-dish observations by Beck et al. (1985), and the error bars reflect the uncertainty in spectral index.

resolution of 0.27 kpc along the major axis. After correction to face-on, the average value of $I_\nu^a(\text{peak})$ sampled by the set of slices is 2.0 ± 0.4 mJy kpc^{-2}, which implies an arm-to-disk contrast $[I_\nu^a(\text{peak}) + I_\nu(\text{disk})]/I_\nu(\text{disk})$ of 3.0 ± 0.8 at $R = 4.3$–7 kpc. The extended emission is patchy on scales greater than several beamwidths, and the quoted value of $I_\nu^a(\text{peak})$ pertains to the emission patches. For $R \lesssim 8.4$ kpc on the eastern arm or $R \lesssim 7.6$ kpc on the western arm, there is no radial trend in the values of $I_\nu^a(\text{peak})$, but thereafter the radio continuum arms decrease in brightness and by $R \cong 9$ kpc are below 3 σ on this VLA map. The lower resolution, higher sensitivity $\lambda = 20$ cm map made by Krause (1987) from VLA D-array observations confirms that the radio arms in M81 become significantly fainter at $R \gtrsim 9$ kpc.

Although we have already argued that the radio continuum arms do not show evidence of the shock present in the H I gas, it is instructive to compare the amplitude trends along the radio continuum and H I arms. On the VLA H I surface-density map, Hine (1984) finds that the amplitudes of the H I arms agree reasonably well with the predicted shock compression in Visser's (1980b) model. For $R \lesssim 8.4$ kpc on the eastern arm or $R \lesssim 7.6$ kpc on the western arm, the radial behavior of the H I arms is similar to that of the radio continuum arms. Then, from there to $R = 9$ kpc the radio continuum arms grow

fainter while the H I arms stay bright until, at least, $R = 11$ kpc. Beyond 9 kpc, the radio continuum arms are quite faint, the optical arms on the younger stars image drop significantly in surface brightness, and no giant radio H II regions are detected (see Figs. 1, 2, 4, and 10 and the colored representations in Kaufman 1987). The contrast in behavior at $R \gtrsim 9$ kpc between the H I arms, on the one hand, and the radio continuum and young-star arms, on the other hand, seems to imply a decrease in the source of cosmic-ray electrons beyond 9 kpc, as one would expect if the electrons are accelerated in SNRs from Population I. Alternatively, we suggest in § VI below that the scale height of the H I gas in the arms may increase beyond $R = 9$ kpc. This would decrease not only the star formation rate but also the strength of the frozen-in magnetic field in the arms and thus produce a decrease in the synchrotron emission.

A highly smoothed view of the arm-to-disk contrast for the extended radio continuum emission is provided by the values of $S_\nu(\text{arm})$ and $S_\nu(\text{disk})$ in Figure 11, where $S_\nu(\text{disk})$ is the axisymmetric flux contribution from the same box as used in the measurement of $S_\nu(\text{arm})$. We find that the average value of the smoothed arm-to-disk contrast $[S_\nu(\text{arm}) + S_\nu(\text{disk})]/S_\nu(\text{disk})$ is 1.6, comparable to the contrast of ~ 2 that Segalovitz (1977) estimates from WSRT observations. Krause, Beck, and Hummel (1989) obtain a similar value for the arm-to-interarm contrast from VLA D-array observations at $\lambda = 20$ cm. The data in Figure 11 show that the smoothed contrast is nearly constant over the range $R = 4.3$–8.2 kpc for the eastern arm, while for the western arm the smoothed contrast is higher at $R < 5.5$ kpc. The portion of the western arm that has a higher smoothed contrast is located in the north, where the arm is broader.

We next consider the average surface brightness ratio $\langle I_\nu(\text{nth})/I_\nu(\text{ff}) \rangle$ of nonthermal to free-free emission in M81 and several other galaxies. From Table 1 we see that at $\lambda = 20$ cm the values of $\langle I_\nu(\text{nth})/I_\nu(\text{ff}) \rangle$ are roughly the same in the spiral arms of M81, M33, and M31, but $\langle I_\nu(\text{nth})/I_\nu(\text{ff}) \rangle$ is greater in the arms of M51 than in the arms of the other galaxies. Since M81 and M31 are early-type spirals whereas M33 and M51 are late-type spirals, this difference does not correlate with morphological type. For the arms of M81, the lower limit to $\langle I_\nu(\text{nth})/I_\nu(\text{ff}) \rangle$ is obtained by assuming that the entire free-free flux density estimated by Beck, Klein, and Krause (1985) originates in the spiral arms; the upper limit is given by setting the free-free flux density equal to just the contribution from the giant radio H II regions. For the arms of M51, the value listed for the surface brightness ratio is a lower limit since the nonthermal component includes only the emission above the base disk.

Let us suppose that the cosmic-ray electrons are accelerated in SNRs. Then, if the cosmic-ray confinement time is the same in all four galaxies, we expect

$$\langle I_\nu(\text{nth})/I_\nu(\text{ff}) \rangle \propto B^{1-\alpha(\text{nth})}, \qquad (7)$$

where B is the magnetic field strength, $\alpha(\text{nth})$ is the spectral index of the nonthermal radio emission, and the constant of proportionality depends on the initial mass function, the frequency, and the electron temperature. We assume here that in the regions compared, the total supernova rate is a constant multiple of the supernova rate in massive stars. The values of B in Table 1 are based on equipartition of energy. To calculate B for the arms of M81, we use the smoothed arm-to-disk contrast ratio of 1.6 for the nonthermal emission and adopt values for

TABLE 1

THE RATIO OF NONTHERMAL TO FREE-FREE SURFACE BRIGHTNESS IN SEVERAL GALAXIES

Galaxy	Feature	$\langle I_\nu(\text{nth})/I_\nu(\text{ff})\rangle$ at 1.465 GHz	B (μG)	$\left(\dfrac{B}{\mu G}\right)^{1-\alpha(\text{nth})}$	Telescope[a]	References
M81	Total, after removal of central source	$\cong 12$	7.5 ± 1.5	35 ± 15	E	1
	Arms, excluding disk surface brightness	0.9–2	...	...	V	2
	Arms, including disk surface brightness	3–5.6	8.5 ± 1.5	44 ± 18	V, E	2
M33	Total	4	3 ± 1	7 ± 5	E	3, 4
	I S arm	2.4–5.5	...	...	E	3
	I N arm	2.0–2.4	...	...	E	3
M31	Total	5 ± 0.6	...	...	E, C	5
	Ring (7–12 kpc)	4 ± 0.5	4 ± 1	14 ± 6	E, C	5, 4
M51	Total	20 ± 9	11 ± 3	120 ± 70	E	6
	Arms, excluding disk surface brightness	7	...	...	V	7

[a] E = Effelsberg 100 m, V = VLA, C = Cambridge One-Mile Synthesis Telescope.

REFERENCES.—(1) Beck, Klein, and Krause 1985; (2) this paper; (3) Berkhuijsen 1983; (4) Beck 1986; (5) Beck and Gräve 1982; (6) Klein, Wielebinski, and Beck 1984; (7) Tilanus *et al.* 1988.

$\alpha(\text{nth})$ and the apparent path length from Beck, Klein, and Krause (1985). For quantities based on the total integrated emission per galaxy, Table 1 shows that the stronger the magnetic field in the galaxy, the greater the value of $\langle I_\nu(\text{nth})/I_\nu(\text{ff})\rangle$, in qualitative agreement with equation (7). Berkhuijsen (1984) finds that SNRs in M33 and M31 can produce enough relativistic electrons to account for the observed nonthermal emission. For M81, M33, and M31, the respective ratios of $\langle I_\nu(\text{nth})/I_\nu(\text{ff})\rangle$ and $B^{1-\alpha(\text{nth})}$ derived from the total integrated emission are consistent with equation (7). Therefore, it appears that acceleration of cosmic-ray electrons in SNRs can explain the integrated nonthermal emission from M81 also.

When comparing the spiral arms, we need to consider the following factors. First of all, the surface brightness ratio $\langle I_\nu(\text{nth})/I_\nu(\text{ff})\rangle$ is greater in a galaxy taken as a whole than in just the spiral arms because the cosmic-ray confinement time is greater for the whole galaxy than for just the spiral arms. On the other hand, density-wave compression increases the magnetic field strength, so the ratio of nonthermal to free-free emission from the arms of different galaxies should tend to correlate with the density wave compression. According to Elmegreen and Elmegreen (1984), the mean value of the arm-to-interarm contrast in surface mass density is approximately 2 (peak-to-trough) in M81 and M33 and approximately 4 in M51. Therefore we expect the value of B in the arms of M81 and M33 to be enhanced by the same factor relative to the mean value of B in the disk. We also predict that the value of $\langle I_\nu(\text{nth})/I_\nu(\text{ff})\rangle$ should be large in the arms of M51, as the observations seem to imply. For the spiral arms of M81, M33, and M31, a comparison of the ratios of $\langle I_\nu(\text{nth})/I_\nu(\text{ff})\rangle$ and $B^{1-\alpha(\text{nth})}$ seems to indicate that the spiral arms of M81 may emit too little nonthermal radiation for the amount of free-free radiation observed. This could be explained if cosmic-ray electrons diffuse out of the arms and into the disk at a greater rate in M81 than in the other two galaxies or if the steepness of the IMF for massive stars differs in these various galaxies.

VI. A COMPARISON BETWEEN THE H I SURFACE DENSITY AND GIANT RADIO H II REGIONS

There are 35 giant radio H II regions on the broad H I arms and six on the H I ring. More than half of the regions on the eastern arm and five on the western arm coincide with the H I ridge line. In M33, Berkhuijsen (1983) and Viallefond and Goss (1986) conclude that H II regions tend to occur in regions of high H I column density. Viallefond, Allen, and Goss (1981) and Viallefond and Goss (1986) point out examples in M101 and M33 of individual H I concentrations that appear associated with H II regions. Although the H II regions in M83 tend to lie along the H I ridge line, Allen, Atherton, and Tilanus (1986) find no detailed coincidence between bright Hβ sources and individual H I concentrations. We are interested in whether there is a relation between giant H II regions and H I column density in M81.

The distribution of H I in the arms of M81 shows structure on various scales, and, like M83, there is usually no clear-cut correspondence between individual H I clouds and individual giant radio H II regions. A similar situation occurs in the central part of M33 (F. Viallefond 1987b, private communication), so when comparing the H II region luminosity with the H I cloud mass in M33, Viallefond and Goss chose isolated H II complexes in less populated areas of the galaxy. For M81, instead of trying to identify associated H II regions and H I clouds, we simply measure the total H I column density N(H I) in the direction of each giant radio H II region and convert to a face-on surface density σ(H I) = N(H I) cos i. The foreground galactic contribution to N(H I) is negligible (Hine 1984), and we assume that the H I gas is optically thin. For each H II region, Table 2 lists the H I column density N(H I), the H I mass M(H I), the Lyman continuum photon flux N_{Lyc}, the mass of ionized gas M(H II), and the ratio A_v/N(H I), where A_v is the visual extinction. The H II region identification number and the values of N_{Lyc} and A_v are taken from Kaufman *et al.*

TABLE 2

GIANT RADIO H II REGIONS IN M81

Source[a] (1)	N(H I) $(10^{21}$ cm$^{-2})$ (2)	M(H I) $(10^6 M_\odot)$ (3)	N_{Lyc} $(10^{50}$ photons s$^{-1})$ (4)	M(H II) $(10^6 M_\odot)$ (5)	$A_v/[0.5N$(H I)] $(10^{-21}$ mag cm$^2)$ (6)
A. H II Regions along the Western Arm					
8	3.0	2.4	2.0	0.3	0.8 ± 0.3
167	2.4	2.0	4.8	0.6	1.1 ± 0.3
159	2.8	3.1	5.5	0.5	0.7 ± 0.2
154	3.1	1.7	1.4	<0.02	0.3 ± 0.4
156	3.0	1.7	3.3	0.1	1.2 ± 0.2
152	2.5	2.7	5.4	0.6	0.2 ± 0.2
135	2.2	0.79	1.3	0.07	1.5 ± 0.5
138	2.4	1.1	5.2	0.3	0.6 ± 0.3
128	2.8	1.6	1.8	<0.03	0.0 ± 0.4
134	1.3	0.46	0.79	0.2	...
137	1.7	0.96	2.0	0.3	0.7 ± 0.6
127	4.0	1.5	1.0	0.04	...
131	2.3	0.81	1.9	0.1	0.4 ± 0.4
121	2.9	1.7	2.8	0.4	0.5 ± 0.3
122	3.5	2.0	2.3	0.2	0.2 ± 0.2
123	3.4	3.8	6.4	0.9	0.5 ± 0.2
202	2.2	0.80	1.0	0.1	...
125	3.1	3.4	5.9	0.6	0.3 ± 0.2
B. H II Regions along the Eastern Arm					
172	2.1	2.3	4.2	0.8	−0.1 ± 0.3
9[b]	0.12	0.04	0.74	0.07	5.0 ± 10.
173	1.4	0.60	1.6	<0.03	5.1 ± 0.7
232	1.9	1.1	1.7	0.2	2.6 ± 0.6
178	3.6	4.0	10.8	1.1	0.8 ± 0.1
5	2.6	1.5	0.94	0.1	...
6	2.1	0.77	0.80	<0.02	...
181	3.2	3.5	11.8	1.1	0.6 ± 0.1
187	3.0	3.3	4.6	0.8	0.3 ± 0.2
104	2.2	1.3	2.3	0.4	1.4 ± 0.4
102	3.4	1.9	2.0	0.4	0.5 ± 0.3
101	3.4	3.8	4.5	0.8	1.2 ± 0.2
197	3.6	3.0	1.9	0.4	0.4 ± 0.3
240	3.9	1.4	1.2	<0.02	1.4 ± 0.3
198	3.3	2.7	3.9	0.5	0.8 ± 0.2
2	2.1	1.7	0.88	0.3	...
229	4.5	1.6	1.0	<0.02	...
185	4.0	2.3	4.6	0.1	0.8 ± 0.2
C. H II Regions along the Inner Ring					
147	1.0	0.36	1.3	0.2	3.6 ± 1.0
1	0.91	1.0	2.4	0.6	0.9 ± 0.9
221	1.2	0.70	1.8	<0.03	3.2 ± 0.8
223	0.95	0.54	1.6	0.2	3.6 ± 1.1
230	1.5	0.52	1.2	0.1	4.1 ± 0.8
228	1.2	0.67	1.4	0.3	2.5 ± 1.0

[a] Source numbers are from Kaufman *et al.* 1987.

[b] Source 9 lies between the eastern arm and the inner ring.

(1987). The mass M(H I) is measured over the same solid angle Ω_s as used in the measurement of N_{Lyc}; N(H I) is the average column density within Ω_s. The values of M(H II) are included in Table 2 simply to show that M(H I) dominates M(H II) for most of the H II regions. We computed the mass M(H II) from the expressions in Panagia and Walmsley (1978) with an assumed electron temperature of 10^4 K. We obtained the deconvolved, equivalent Gaussian sizes required for this calculation either from the Hα map (resolution = 10″) used by Kaufman *et al.* for measuring the integrated Hα flux of each source or, in the case of sources with small diameter, from an Hα map with a resolution of ∼4″. In some cases, Gaussians gave a poor fit to the intensity distribution. The maximum

value of the deconvolved angular diameter (FWHM) in this set of H II regions is 13″ (200 pc), but several regions are totally unresolved. For the values of M(H II) listed in Table 2, we set the volume filling factor f equal to 1. Except for one interarm region (No. 9), M(H I) clearly exceeds M(H II). In fact, since M(H II) scales as $f^{1/2}$, and, according to Kennicutt (1984) and O'Dell and Castenda (1984), f is typically 0.01–0.1 in giant H II regions in nearby galaxies, the values listed for M(H II) should be regarded as upper limits. We conclude that we can neglect the mass of the ionized component compared to M(H I) for the giant radio H II regions on the spiral arms.

To avoid the uncertainty associated with the filling factor, we compare the H I data with the Lyman continuum flux N_{Lyc}
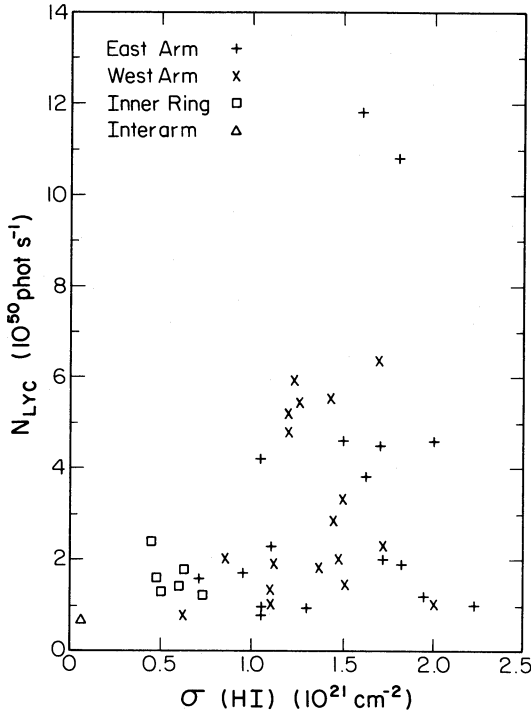
FIG. 12.—Comparison between the Lyman continuum photon flux and the face-on surface density of H I in the direction of each giant radio H II region.

$N_{Lyc} < 2.5 \times 10^{50}$ photons s^{-1}). For the most part, these are H II regions on the inner H I ring. The majority of the H II regions on the eastern and western arms have σ(H I) in the rather narrow range $1-2 \times 10^{21}$ atoms cm^{-2}. The H II regions on the arms show no systematic dependence of N_{Lyc} on σ(H I); i.e., the correlation coefficient = 0.3. Aside from the one inter-arm region in the set, it appears that the minimum H I surface density associated with a giant radio H II region in M81 is 0.5×10^{21} atoms cm^{-2}. The situation for the H II regions in M33 is similar: the 43 H II regions studied by Viallefond and Goss (1986) have σ(H I) = $0.6-1.6 \times 10^{21}$ atoms cm^{-2}, and within this range there is no apparent relation between N_{Lyc} and σ(H I). Thus, for the giant radio H II regions in M81 and the H II regions in M33, σ(H I) lies in the same narrow range: $0.5-2 \times 10^{21}$ atoms cm^{-2}. This suggests that the formation of a massive OB association is governed by a certain threshold surface density of gas. The threshold value is probably deter-mined by the self-shielding required to form a molecular core in a giant cloud.

The suggested scenario is that once the gas surface density in a giant cloud exceeds a critical value, the core of the cloud becomes molecular and then may give birth to OB stars. Although ionization by the OB stars tends to deplete the amount of H I, this does not significantly decrease the total σ(H I) in the direction of the H II region because only a small fraction of the mass is ionized. According to Elmegreen (1988), a diffuse cloud in the solar neighborhood has sufficient self-shielding to become molecular when the product σ(H I) n(H I) exceeds 2×10^{22} cm^{-5}, where n(H I) is volume density of H I. The σ(H I) values that we find in the directions of the giant radio H II regions in M81 are typical of the peak H I concentra-tions along the arms in M81 (see the contour plot in Fig. 13) and along the arms in our Galaxy (Kulkarni, Blitz, and Heiles

rather than with the mass M(H II). Figure 12 describes the correspondence between the face-on surface density σ(H I) and N_{Lyc}. All the H II regions with σ(H I) less than 10^{21} atoms cm^{-2} are at the lower end of the luminosity distribution (i.e.,
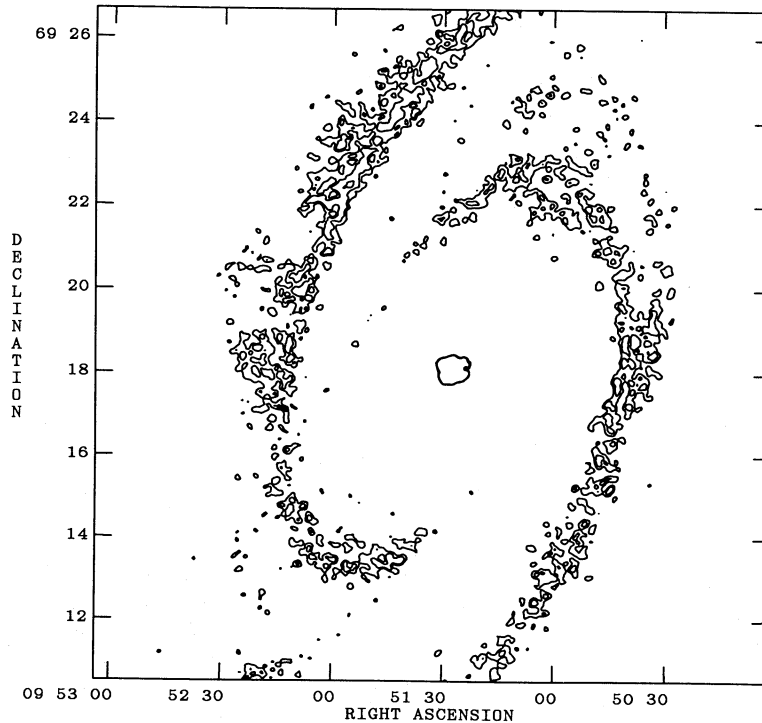

FIG. 13.—Plane-of-sky plot of the H I surface density with contour levels chosen to show just the peak concentrations of H I. The contour levels are at N(H I) = 2.5 and 3.75 $\times 10^{21}$ atoms cm^{-2} (20 and 30 $M_\odot$ pc^{-2}). If corrected to face-on, these levels correspond to σ(H I) = 1.3 and 1.9 $\times 10^{21}$ atoms cm^{-2}.

1982) and are close to the estimated threshold surface density σ_c for converting H I to H_2 in our Galaxy and in the 10 kpc ring in M31 (Lada 1988): $\sigma_c = 6 \times 10^{20}$ atoms cm^{-2} for local diffuse clouds and 10^{21} atoms cm^{-2} for the 10 kpc ring in M31. We expect σ_c to be somewhat greater in the arms of M81 than in the M31 ring because the UV radiation field is more intense in the M81 arms. In § VII we shall use a comparison of N(H I) and the visual extinction A_v to infer information about the molecular material. We find that, with the exception of the H II regions on the inner ring, the gas in the direction of the typical giant radio H II region is primarily in the form of H I.

Since the molecular contribution is small for nearly all of the H II regions on the spiral arms in M81, we take the luminosity efficiency as N_{Lyc}/M(H I). This approximation is not appropriate for the H II regions on the inner ring: the inner ring sources contain more molecular hydrogen (see § VII) and, consequently, they have relatively high values of N_{Lyc}/M(H I) (see Fig. 14). If we omit the inner ring H II regions, then most of the H II regions in Figure 14 fall in the range N_{Lyc}/M(H I) $= 0.5$–2.5 $\times 10^{44}$ photons s^{-1} $M_\odot^{-1}$. The solid curve in this figure is a power-law fit to the data and can be understood as resulting from the absence of correlation between N_{Lyc} and σ(H I) plus the definition of M(H I) as the H I mass within the solid angle subtended by the H II region.

We find an average luminosity efficiency for giant radio H II regions in M81 that is a factor of 2 or 3 below the values obtained by Viallefond and Goss (1986) and Viallefond (1987a) for isolated giant H II regions in M33 and in blue compact galaxies. However, Viallefond and coworkers use a definition of M(H I) that differs from our definition; i.e., they identify the H I cloud, which is not necessarily coextensive with the H II region; we measured the average H I column density through the galaxy in the direction of the H II region. Therefore, the difference in luminosity efficiency between the H II regions in M81 and in their samples should not be treated as significant.

On the other hand, it is clear from examination of Figures 4, 13, 15, and 16 that there are clumps with σ(H I) $> 10^{21}$ atoms cm^{-2} but with no associated giant H II region. (The dust lanes marked on Figs. 15 and 16 serve as a guide to the eye in comparing positions.) First, we discuss the situation at $R > 9$ kpc: although the H I surface density in the arms is large here,
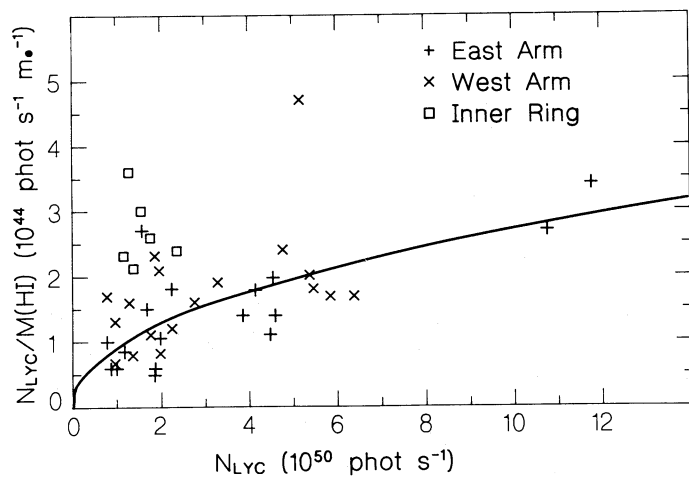
no giant radio H II regions are detected, and the arms on the younger stars image are faint. This behavior is typical of the outer parts of spiral galaxies. Note that a high surface density of H I does not necessarily mean a high volume density of H I. For example, Kulkarni, Blitz, and Heiles (1982) find that in our Galaxy σ(H I) is roughly constant on the spiral arms out to 20 kpc, but the H I scale height increases by at least a factor of 3 between $R = 10$ and 20 kpc. This is significant because the formation of giant clouds and large OB associations presumably depends on the local volume density of gas as well as on the column density. The increase in scale height implies a decrease in the number of small clouds per unit volume, which is important if giant clouds are produced by the agglomeration of small clouds. While we have no information about how the H I scale height varies in M81, if the scale height increases appreciably beyond $R = 9$ kpc, this may explain the absence of large OB associations in the outer part of the galaxy.

In the region $R = 5$–8 kpc, where we presume that the H I scale height is constant, we can interpret column density peaks as volume density peaks. Even in this part of M81, there are H I concentrations with a high gas surface density but with no associated giant H II region. Viallefond (1987a) finds a similar situation in the galaxies he has studied and interprets this as indicating a long time delay before massive star formation turns on. An alternative interpretation is that something besides just the density of gas controls the formation of giant clouds and the formation of OB associations. The extra ingredient may be cloud collisions, as suggested by a number of authors; the cloud collision rate, in turn, is increased by orbit crowding in the arms.

VII. THE NATURE OF THE GAS IN THE DIRECTIONS OF THE GIANT RADIO H II REGIONS

We want to find out if the gas in the directions of the giant radio H II regions in M81 is primarily H I or primarily H_2. Since CO emission from M81 is very weak (Brouillet, Baudry, and Combes 1988), we rely instead on extinction measurements to search for H_2. High-resolution information about the distribution of molecular gas can be obtained from A_v values by comparing the visual extinction with the H I column density, since excess extinction would be evidence for molecular gas. This involves some assumption about the relative geometry, because A_v is measured in front of a bright source, while N(H I) is the total column density through the galaxy. We now describe the results of A_v/N(H I) measurements in the directions of the giant radio H II regions.

Kaufman et al. (1987) have determined A_v in the directions of the giant radio H II regions by comparing radio continuum flux densities and Hα fluxes. We consider whether the H I column density, by itself, is sufficient to explain the observed extinction. Since we expect that, on average, the H II regions should be located at the midplane, we set the gas column density N_{gas} equal to half the measured H I column density N(H I). The observed values of A_v and N(H I) both pertain to the same solid angle. Figure 17 shows the ratio A_v/N_{gas} in the directions of the giant radio H II regions on the spiral arms and the inner ring. Some of the scatter results because A_v depends on where the H II region is situated relative to the midplane.

The dashed curves in Figure 17 give the predicted variation of A_v/N_{gas} with galactocentric radius for H II regions on the midplane and for those at the extreme far and near edges of the gas layer. To obtain the predicted curves, we used the O/H abundance gradient derived by Garnett and Shields (1987) for

FIG. 14.—The luminosity efficiency N_{Lyc}/M(H I) of the giant radio H II regions on the spiral arms and on the inner ring. Solid curve shows a power-law fit to the data if the H II regions on the inner ring are omitted.
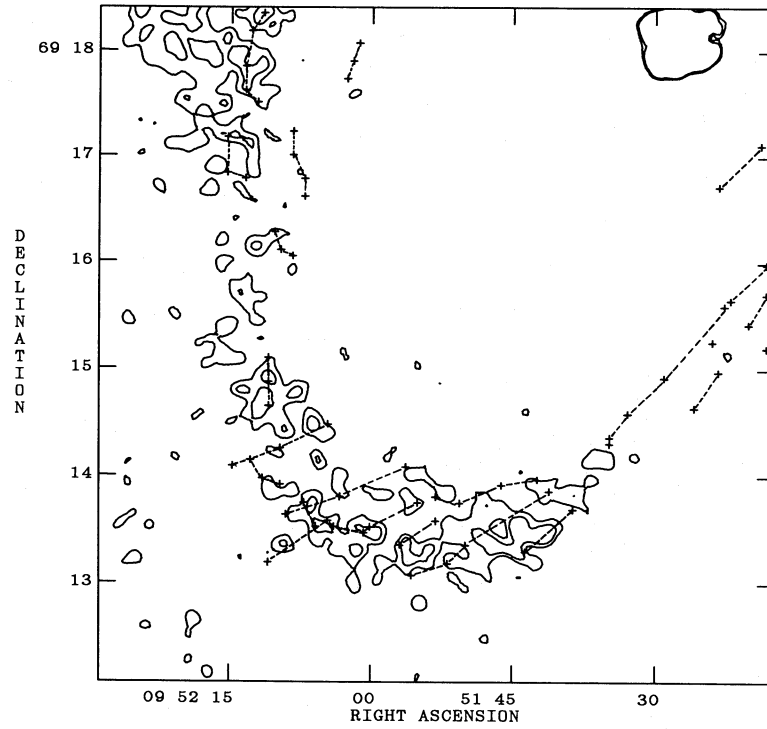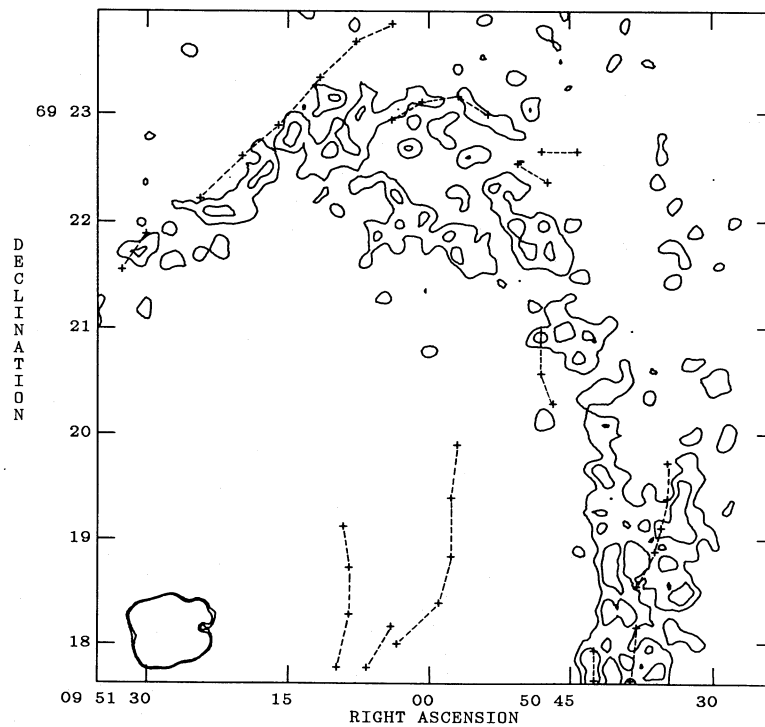
FIG. 15a

FIG. 15b

FIG. 15.—(a, b) Plane-of-sky contour plots of the H I surface density with the dust lanes marked as plus (+) signs connected by dashed lines. H I contour levels are the same as in Fig. 13. The dust lanes are marked here and in Fig. 16 to serve as a guide to the eye in comparing the positions of the H I concentrations with the positions of the giant radio H II regions shown in Fig. 16. Some of the dust filaments cut across regions of high H I column density, but only a few dust features follow the H I ridge line.

PEAK FLUX = 5.0741E+00
LEVS =   5.0000E-01 * (1.000, 1.500, 3.000,
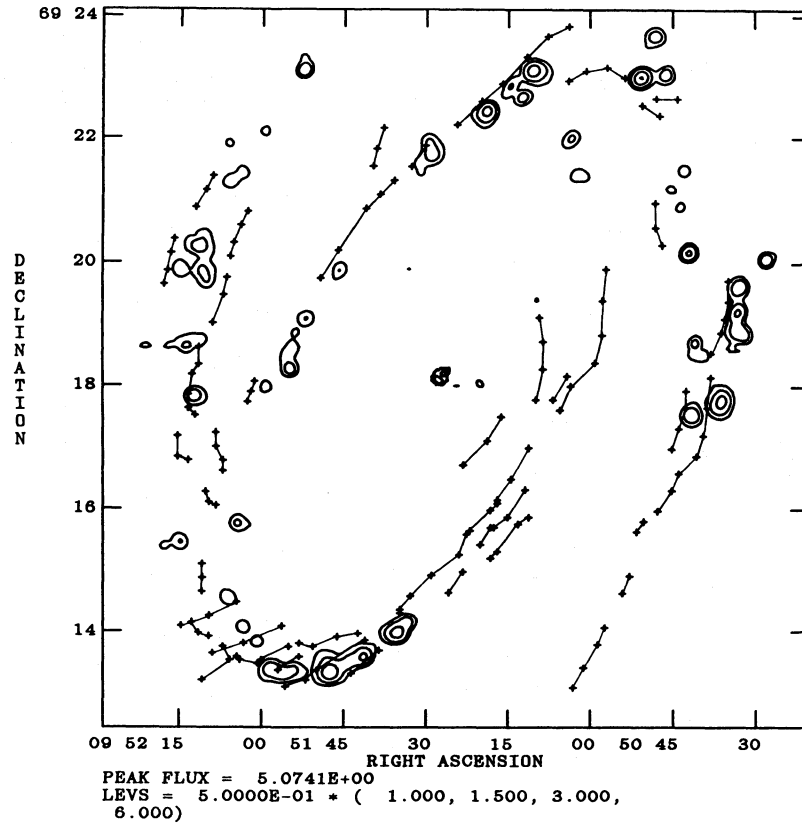   6.000)

FIG. 16.—Plane-of-sky contour plot of the giant radio H II regions with the dust lanes marked as plus (+) signs connected by lines
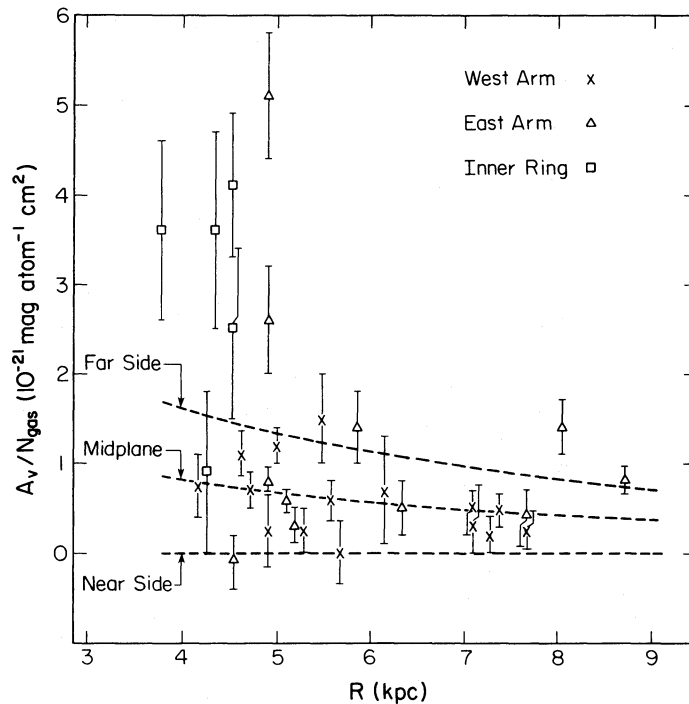

FIG. 17.—Comparison between the observed values of A_v/N_{gas} for the giant radio H II regions (*symbols with error bars*) and the predicted values of A_v/N_{gas} (*dashed curves*) for H II regions on the midplane and at the extreme near and far edges of the gas layer. The column density N_{gas} for the predicted curves includes both H I and H_2, whereas N_{gas} for the observed points includes only H I. An observed point will lie in the part of the diagram bounded by the dashed curves if the column density of H_2 is small compared to that of H I.

M81 to scale the standard galactic value, $A_v/N_{gas} = 0.53 \times 10^{-21}$ mag per atom cm^{-2} (Bohlin, Savage, and Drake 1978), to the O/H abundances in M81. That is, we set

$$\frac{A_v}{N_{gas}} = 0.53 \times 10^{-21} \text{ mag per atom cm}^{-2} \frac{O/H}{(O/H)_{local}}. \quad (11)$$

We take log $(O/H)_{local} + 12 = 8.70 \pm 0.04$ from Shaver *et al.* (1983) for the H II regions in the solar vicinity, and we fit a smooth curve to the values of O/H measured by Garnett and Shields for the H II regions in M81. Whereas N_{gas} for the predicted curves includes both H I and H$_2$, N_{gas} for the observed points represents solely the H I gas. Therefore an observed point will lie in the part of the diagram bounded by the dashed curves if the column density of H$_2$ is small compared to the column density of H I.

For the giant H II regions on the eastern and western arms, the observed distribution of A_v/N_{gas} has the following properties: (*a*) roughly equal numbers of H II regions fall above and below the predicted midplane curve; (*b*) 90% of the regions lie in the part of the diagram corresponding to negligible H$_2$; (*c*) in fact, 40% have A_v/N_{gas} values consistent with a midplane location and negligible H$_2$. For such regions, most of the H$_2$ gas in the cloud prior to the onset of OB star formation must have dissociated. However, seven relatively low luminosity regions (four on the inner ring and three on the eastern arm) lie significantly above the predicted curves; these have too much extinction for the amount of H I. Even if we also include in N_{gas} the ionized component with a volume filling factor of 1 (to obtain an upper limit), we still find that five of these regions have too much extinction unless the contribution from H$_2$ is significant. We conclude that for most of the set of H II regions, the column density of H$_2$ in the direction of the H II region is negligible, but in a few cases, an appreciable column density of H$_2$ seems to be required. We note that all the H II regions with an important inferred molecular contribution have relatively low Lyman continuum luminosities (i.e., have $N_{Lyc} < 1.8 \times 10^{50}$ photons s^{-1}). Thus the more luminous H II regions are more effective either in dissociating the molecular gas or in pushing it out of the solid angle subtended by the H II region. The H II regions in M81 are efficient in destroying molecular gas because the average A_v for the H II regions on the arms is only 1.0 ± 0.4 mag.

One possible source of systematic error in the A_v values is that Kaufman *et al.* (1987) assume an electron temperature T_e of 10^4 K. For 13 of the H II regions, Garnett and Shields (1987) provide T_e values from optical line ratios, but these were measured with a 4″ aperture, which is small compared to the size of most of the giant radio H II regions. Nevertheless, if we adopt their T_e values, then the average value of A_v increases by 0.2 mag, which is less than the measurement uncertainty in A_v. An increase in A_v of 0.2 mag corresponds to an increase in N_{gas} of $2-5 \times 10^{20}$ atoms cm^{-2}, or 9%–19% of the average H I column density associated with the giant radio H II regions on the spiral arms. It does not change the number of H II regions that lie appreciably above the far-side curve in Figure 17, and therefore does not alter our conclusions.

Thus we deduce that the gas in the direction of a typical giant radio H II region on the arms is primarily H I. Because the H I column densities in the directions of the giant radio H II regions are about the same as elsewhere along the spiral arms (see § VI), we confirm the suggestion by Kaufman *et al.* (1987) that the extinction they measure for the H II regions represents

the general level of extinction within the spiral arms, not something peculiar to the H II regions. As an aside, we note that there is a 1.5–2 mag difference in A_v between H II regions at the extreme near and far edges of the H I gas layer. This has an important implication for distance estimates of M81 (or other spiral galaxies) that use luminosity indicators on the spiral arms. Unless the extinction of the luminosity indicator is measured, the derived distance modulus may be uncertain by 0.75–1 mag.

The values of A_v in the directions of the giant radio H II regions also allow us to sample the distribution of extinction across the arms. One common notion about the grand design spirals is that the dust lanes lie along the inside edge of the arm at the position of the spiral shock front. Also, Allen, Atherton, and Tilanus (1986) suggest that in M51 and M83 the interstellar gas is primarily molecular until dissociated by star formation in the arm. If these descriptions were to apply to M81, then we should expect to find a cross-arm gradient in A_v or in $A_v/N(H\ I)$. Table 3 indicates that there is no tendency for either A_v or $A_v/N(H\ I)$ to be greater for regions closer to the shock front. In this table, d is the perpendicular distance defined by equation (6), $n_{H\ II}$ is the sample size, the error bars listed in columns (3) and (5) are the measurement uncertainties, "s.e." is the dispersion in the mean value, $\langle A_v \rangle$, and n_{SG} is the number of supergiant H II regions in the sample. We conclude that the dust is spread across a broad compression zone. This resembles the broad molecular cloud collision front predicted by Elmegreen (1988) for galaxies with moderate-amplitude density waves, except that the clouds sampled here seem to be mainly atomic rather than molecular.

Kaufman *et al.* (1989) make a detailed analysis of the dust filaments that are plotted here in Figures 3*c*, 9, 15, and 16. They find that the dust filaments near the spiral velocity shock front have neither greater length nor greater extinction than the filaments farther downstream. They conclude that narrow dust filaments composed primarily of molecular gas are spread over a zone that starts near the spiral shock front and extends 1.5 kpc downstream. This type of dust lane morphology agrees with the cross-arm distribution of dust sampled by the giant radio H II regions. The absence of a major, high-opacity dust lane along the velocity shock front seems consistent, also, with the weakness of the CO emission from M81.

VIII. CONCLUSIONS

The following common notions about grand design spirals appear in the literature (e.g., Duric 1986): (*a*) long continuous dust lanes lie along the spiral shock front; (*b*) the enhanced synchrotron arm emission comes from the spiral shock front; (*c*) the arrangement of stars and dust in a spiral arm forms a

TABLE 3

CROSS-ARM DISTRIBUTION OF EXTINCTION SAMPLED BY THE GIANT RADIO
H II REGIONS

d (kpc) (1)	$n_{H\ II}$ (2)	$\langle A_v \rangle$ (mag) (3)	s.e. (mag) (4)	$\langle A_v/0.5\ N(H\ I) \rangle$ (10^{-21} mag cm^2) (5)	n_{SG} (6)
-1.0 to -0.5....	1[a]	0.3 ± 0.6	...	$10. \pm 5.$	0
-0.5 to 0.0.......	1	1.1 ± 0.5	...	0.8 ± 0.3	0
0.0 to 0.5..........	3	1.1 ± 0.5	0.7	1.0 ± 0.4	0
0.5 to 1.0..........	12	1.1 ± 0.4	0.3	1.0 ± 0.3	6
1.0 to 1.5..........	8	0.8 ± 0.3	0.2	0.6 ± 0.2	5
1.5 to 2.0..........	2	1.6 ± 0.5	1.1	1.1 ± 0.5	0

[a] This is the one interarm H II region in the set.

sequence in the downstream direction consisting of first the dust lane, then the H II regions, and then the red arms. Although M81 has long, symmetric spiral arms and is a classic example of a density-wave galaxy, it has none of the above characteristics. Instead, we find the following features:

1. The H I gas, the nonthermal radio emission, the dust and the narrow dust filaments, the young stars, and the giant radio H II regions are each distributed across a broad spiral compression zone that starts near the measured position of the spiral velocity shock front and extends 1–2 kpc downstream from the shock front.

2. Since the arm-to-interarm contrast in surface mass density is appreciable, we find that old stars and young stars both collect near the gravitational potential minimum on the arms.

3. The evidence favors an SNR origin for the cosmic-ray electrons that produce the nonthermal radio arms. Namely:

   a) The radio continuum arms are roughly centered on the ridge of young stars and the gravitational potential minimum, not on the velocity shock front;

   b) The radio continuum arms are broad, spread out like the stellar arms;

   c) The ratio of nonthermal to free-free emission is comparatively low, and therefore SNRs can produce enough cosmic-ray electrons to account for the nonthermal emission;

   d) The radio continuum arms and the arms defined by the young stars are similar in that both drop significantly in surface brightness beyond 9 kpc, whereas the H I arms remain bright until, at least, $R = 11$ kpc.

4. The location of an H II region above or below the midplane provides a satisfactory explanation of the observed dispersion in the values of the visual extinction A_v for the set of giant radio H II regions. We predict a 1.5–2 mag difference in A_v between objects located at the extreme near and far edges of the H I gas layer on the spiral arms.

5. The cross-arm distribution of extinction sampled by the H II regions shows no tendency for either A_v or $A_v/\sigma(H\ I)$ to be greater closer to the shock front, where $\sigma(H\ I)$ is the face-on surface density of H I. This agrees with the observed dust lane morphology: Kaufman, Elmegreen, and Bash (1989) find that (1) there is no prominent, long, high-opacity dust lane at the velocity shock front, and (2) narrow dust filaments are spread over a zone that starts near the velocity shock front and extends 1.5 kpc downstream. The absence of a major dust lane along the shock front seems consistent with the weakness of the CO emission from M81.

6. Although Roberts and coworkers need to calculate a model with input parameters appropriate to M81, it appears that the observed compression zone in M81 resembles the broad compression zone predicted in their cloudy density-wave model for the Milky Way. In particular, we find the following points of agreement between the observations of M81 and their cloudy model:

   a) The observed width of the compression zone is close to the predicted width.

   b) The downstream displacement of the H I ridge from the velocity shock front is comparable to the predicted thickness of the "shock front" in their model.

c) The observed near-coincidence between the young star ridge and the potential minimum agrees with their predictions.

d) The cloudy model by Roberts and coworkers seems to be more successful than the cloudy model by Leisawitz and Bash (1982) in accounting for the observed distribution of giant radio H II regions across the spiral arms. The observed distribution supports the notion that orbit crowding near the potential minimum plays an important role in producing the massive OB associations.

e) The absence of a major, high-opacity dust lane along the velocity shock front is consistent with the cloudy model by Roberts and coworkers.

Thus many of the general features of the spiral arms in M81 can be explained by density-wave models that emphasize the clumpy nature of the interstellar medium.

7. For the giant radio H II regions on the arms, the H I column density measured in the direction of the H II region is usually sufficient, by itself, to explain the observed extinction of the H II region. Therefore the high-luminosity H II regions either dissociate most of the molecular gas in the cloud or drive it out of the solid angle subtended by the H II region.

8. The luminosity efficiency of giant H II regions in M81 agrees within a factor of a few with that found in M33 and blue compact galaxies. For H II regions in M81 and M33, the face-on surface density of H I measured in the direction of each giant radio H II region lies in the narrow range $\sigma(H\ I) = 0.5–2 \times 10^{21}$ atoms cm^{-2}. We regard this as observational evidence that the birth of a massive OB association involves a threshold surface density of gas. Nevertheless, there are H I concentrations with $\sigma(H\ I)$ in the same range but with no associated giant radio H II region. This suggests that some other factor, such as orbit crowding and cloud collisions, also plays an important role in the formation of giant clouds and massive OB associations. Furthermore, the absence of large OB associations in the outer part of M81 can be understood if the H I scale height were to increase appreciably beyond $R = 9$ kpc.

REFERENCES

Allen, R. J. 1988, in *Applied Mathematics, Fluid Mechanics, and Astrophysics: A Symposium to Honor C.C. Lin*, ed. D. J. Benney, F. H. Shu, and C. Yuan (Singapore: World Scientific), p. 299.
Allen, R. J., Atherton, P. D., and Tilanus, R. P. J. 1986, *Nature*, **319**, 296.
Bash, F. N., and Kaufman, M. 1986, *Ap. J.*, **310**, 621.
Beck, R. 1986, *IEEE Trans. Plasma Science*, **PS-14**, 740.
Beck, R., and Gräve, R. 1982, *Astr. Ap.*, **105**, 192.
Beck, R., Klein, U., and Krause, M. 1985, *Astr. Ap.*, **152**, 237.
Berkhuijsen, E. M. 1983, *Astr. Ap.*, **127**, 395.
———. 1984, *Astr. Ap.*, **140**, 431.
Bohlin, R. C., Savage, B. D., and Drake, J. F. 1978, *Ap. J.*, **224**, 132.
Bottinelli, L., Gouguenheim, L., Paturel, G., and de Vaucouleurs, G. 1984, *Astr. Ap. Suppl.*, **56**, 381.
Brouillet, N., Baudry, A., and Combes, F. 1988, *Astr. Ap.*, **196**, L17.
Combes, F., and Gerin, M. 1985, *Astr. Ap.*, **150**, 327.
Duric, N. 1986, *Ap. J.*, **304**, 96.
Elmegreen, B. G. 1987, in *IAU Symposium 115, Star Forming Regions*, ed. M. Peimbert and J. Jugaku (Dordrecht: Reidel), p. 457.
———. 1988, *Ap. J.*, **326**, 616.
Elmegreen, D. M. 1981, *Ap. J. Suppl.*, **47**, 229.
Elmegreen, D. M., and Elmegreen, B. G. 1984, *Ap. J. Suppl.*, **54**, 127.
Garnett, D. R., and Shields, G. A. 1987, *Ap. J.*, **317**, 82.
Hausman, M. A., and Roberts, W. W., Jr. 1984, *Ap. J.*, **282**, 106.
Hine, B. 1984, M.A. thesis, University of Texas.
Hine, B., and Rots, A. H. 1989, in preparation.
Kaufman, M. 1987, *Sky and Telescope*, **73**, 135.
Kaufman, M., and Bash, F. N. 1987, in *Star Formation in Galaxies*, ed. C. J. Persson (NASA Conf. Pub. 2466), p. 227.
Kaufman, M., Bash, F. N., Kennicutt, R. C., Jr., and Hodge, P. W. 1987, *Ap. J.*, **319**, 61.
Kaufman, M., Elmegreen, D. M., and Bash, F. N. 1989, *Ap. J.*, in press.
Kennicutt, R. C., Jr. 1984, *Ap. J.*, **287**, 116.
Klein, U., Wielebinski, R., and Beck, R. 1984, *Astr. Ap.*, **135**, 213.
Krause, M. 1987, Ph.D. thesis, University of Bonn.
Krause, M., Beck, R., and Hummel, E. 1987, in *Proc. Interstellar Magnetic Fields*, ed. R. Beck and R. Gräve (Berlin: Springer), p. 57.
———. 1989, *Astr. Ap.*, in press.

Kulkarni, S., Blitz, L., and Heiles, C. 1982, *Ap. J. (Letters)*, **259**, L63.
Lada, C. J. 1988, in *Galactic and Extragalactic Star Formation*, ed. R. E. Pudritz and M. Fich (Dordrecht: Reidel), p. 5.
Leisawitz, D., and Bash, F. N. 1982, *Ap. J.*, **259**, 133.
Lubow, S. H., Balbus, S. A., and Cowie, L. L. 1986, *Ap. J.*, **309**, 496.
O'Dell, C. R., and Castenada, H. O. 1984, *Ap. J.*, **283**, 158.
Oort, J. H. 1974, in *IAU Symposium 58, The Formation and Dynamics of Galaxies*, ed. J. R. Shakeshaft (Dordrecht: Reidel), p. 375.
Panagia, N., and Walmsley, C. M. 1978, *Astr. Ap.*, **70**, 411.
Roberts, W. W., Jr. 1969, *Ap. J.*, **158**, 123.
Roberts, W. W., Jr., Adler, D. S., and Stewart, G. R. 1988, in *Applied Mathematics, Fluid Mechanics, and Astrophysics: A Symposium to Honor C. C. Lin*, ed. D. J. Benney, F. H. Shu, and C. Yuan (Singapore: World Scientific), p. 373.
Roberts, W. W., Jr., and Hausman, M. A. 1984, *Ap. J.*, **277**, 744.
Roberts, W. W., Jr., and Stewart, G. R. 1987, *Ap. J.*, **314**, 10.
Rots, A. H. 1975, *Astr. Ap.*, **45**, 43.
Schweizer, F. 1976, *Ap. J. Suppl.*, **31**, 313.
Segalovitz, A. 1977, *Astr. Ap.*, **55**, 203.
Shaver, P. A., McGee, R. X., Newton, L. M., Danks, A. C., and Pottasch, S. R. 1983, *M.N.R.A.S.*, **204**, 53.
Tilanus, R. P. J., Allen, R. J., van der Hulst, J. M., Crane, P. C., and Kennicutt, R. C., Jr. 1988, *Ap. J.*, **330**, 667.
Tomisaka, K. 1987, in *IAU Symposium 115, Star Forming Regions*, ed. M. Peimbert and J. Jugaku (Dordrecht: Reidel), p. 541.
van Albada, G. D. 1985, *Astr. Ap.*, **142**, 491.
Viallefond, F. 1987a, in *Galactic and Extragalactic Star Formation*, ed. R. Pudritz and M. Fich (Dordrecht: Reidel), p. 439.
———. 1987b, private communication.
Viallefond, F., Allen, R. J., and Goss, W. M. 1981, *Astr. Ap.*, **104**, 127.
Viallefond, F., and Goss, W. M. 1986, *Astr. Ap.*, **154**, 357.
Visser, H. C. D. 1978, Ph.D. thesis, University of Groningen.
———. 1980a, *Astr. Ap.*, **88**, 149.
———. 1980b, *Astr. Ap.*, **88**, 159.
Vogel, S. N., Kulkarni, S. R., and Scoville, N. Z. 1988, *Nature*, **334**, 402.
Zwicky, F. 1955, *Pub. A.S.P.*, **67**, 232.

FRANK N. BASH: Department of Astronomy, University of Texas at Austin, Austin, TX   78712

DEBRA M. ELMEGREEN: Vassar College Observatory, Poughkeepsie, NY   12601

BUTLER HINE: NASA/Ames Research Center, MS 245-3, Moffett Field, CA   94035

PAUL W. HODGE: Astronomy Department, FM-20, University of Washington, Seattle, WA   98195

MICHELE KAUFMAN: Department of Physics, Ohio State University, 174 West 18th Avenue, Columbus, OH   43210

ARNOLD H. ROTS: NRAO, P.O. Box O, Socorro, NM   87801